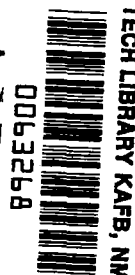


NASA
RP
1034
c.1

NASA Reference Publication 1034

LOAN COPY: RETURN *
AFWL TECHNICAL LIBRARY
KIRTLAND AFB, N. M.



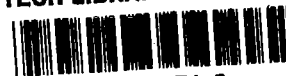
Convective Rainfall Estimation From Digital GOES-1 Infrared Data

Gary L. Sickler and Aylmer H. Thompson

SEPTEMBER 1979

NASA





NASA Reference Publication 1034

Convective Rainfall Estimation From Digital GOES-1 Infrared Data

Gary L. Sickler and Aylmer H. Thompson
Texas A&M University
College Station, Texas

Prepared for
George C. Marshall Space Flight Center
Marshall Space Flight Center, Alabama



National Aeronautics
and Space Administration

Scientific and Technical
Information Branch

1979

ACKNOWLEDGMENTS

The authors express appreciation to Drs. K. C. Brundidge, G. L. Huebner, W. M. Lively, and V. E. Moyer for reviewing and providing constructive comments on the manuscript. Captain Rod Henderson, Mr. Ray McAnelly, and Mr. Stan Thiessen helped immensely by providing data, maps, other material, and many valuable suggestions. Their help is gratefully acknowledged.

TABLE OF CONTENTS

	Page
LIST OF TABLES.	iv
LIST OF FIGURES	v
1. INTRODUCTION.	1
2. BACKGROUND.	3
3. THE GOES-1 SYSTEM	9
4. DATA.	18
a. Raingage Data	18
b. Digital GOES-1 Data	19
c. Supplemental Data	20
5. RESULTS	21
a. The Synoptic Situation.	21
b. The Raingage Analysis	27
c. The Satellite Analysis.	30
d. The Satellite-Derived Rainfall Estimations.	56
e. Comparisons	66
6. CONCLUSIONS	73
7. RECOMMENDATIONS	76
REFERENCES.	78
APPENDIX A.	81
APPENDIX B.	85

LIST OF TABLES

Table		Page
1	Current SFSS's in operation.	12
2	Hourly rainfall amounts and 3-h/24-h total rainfall in mm.	29
3	Digital count/observed rainfall for the northwest quadrant during the second hour.	35
4	Hourly rainfall estimates and 3-h total in mm.	65
5	Hourly and 3-h observed and estimated rainfall in mm . .	70

LIST OF FIGURES

Figure		Page
1	Assembly of VISSR mode A picture data showing the relationship between infrared and visible sensor lines.	11
2	GOES data flow diagram	13
3	Standard IR calibration of digital count values to their associated equivalent blackbody temperatures . . .	15
4	M _B enhancement curve	17
5	Area under investigation with CLL located at the center.	22
6a	NWS surface analysis at 0000 GMT, May 3, 1978.	23
6b	300 mb upper level wind at 0000 GMT, May 3, 1978	23
7	NWS radar summary at 0135 GMT, May 3, 1978	25
8	NWS radar summary at 0235 GMT, May 3, 1978	26
9	24-h rainfall analysis in mm for a 240 km by 240 km box centered on CLL.	28
10	First hour rainfall analysis in mm	31
11	Second hour rainfall analysis in mm.	32
12	Third hour rainfall analysis in mm	33
13	3-h total rainfall in mm	34
14	Digital count value map at 03/0045 GMT	37
15	0100 GMT GOES-1 M _B EIR image	38
16a	DCVM at 03/0100 GMT.	39
16b	DCVM at 03/0115 GMT.	40
16c	DCVM at 03/0130 GMT.	41
16d	DCVM at 03/0145 GMT.	42
17	0200 GMT GOES-1 M _B EIR image	43
18a	DCVM at 03/0200 GMT.	44

LIST OF FIGURES (CONCL'D)

Figure	Page
18b DCVM at 03/0215 GMT.	45
19 0230 GMT GOES-1 M_B EIR image	46
20a DCVM at 03/0230 GMT.	47
20b DCVM at 03/0245 GMT.	48
21 0300 GMT GOES-1 M_B EIR image	50
22a DCVM at 03/0300 GMT.	51
22b DCVM at 03/0315 GMT.	52
22c DCVM at 03/0330 GMT.	53
22d DCVM at 03/0345 GMT.	54
23 0400 GMT GOES-1 M_B EIR image	55
24 Rainfall in $\text{mm } \frac{1}{4}\text{h}^{-1}$ based on the growth or decay of the area of digital count value.	58
25 The satellite-derived rainfall estimation analysis for the first hour	60
26 The satellite-derived rainfall estimation analysis for the second hour.	61
27 The satellite-derived rainfall estimation analysis for the third hour	62
28 The 3-h total of satellite-derived rainfall estimation analyses	64
29 The 0223 GMT total VIL map superimposed on the displaced 0230 GMT DCVM.	71
30 Rainfall in $\text{mm } \frac{1}{4}\text{h}^{-1}$ based on the growth or decay of the area of digital count value.	83
31 Diagram illustrating an actual versus an apparent cloud location	86
32 Dimensions used in calculating cloud location corrections.	86

1. INTRODUCTION

Manmade satellites have provided data for some of the more important scientific contributions of our century, and quite justifiably mankind should have great admiration for those whose ingenuity and imagination have made them possible. Yet long before the Wright Brothers accomplished their historic flight at Kitty Hawk, long before Fulton engineered the steamboat, and even before James Watt unraveled the principles behind the steam engine, a man named Isaac Newton considered the possibilities of satellites and outlined the conditions necessary to make them possible. Three hundred years ago, in Principia Mathematica, Newton discussed the conditions under which a projectile must be launched to follow a specific orbit and laid the precise mathematics of orbital motion. Newton foresaw rocket propulsion and was able to state the theory behind it. Over three centuries ago, Isaac Newton understood the mathematic principles that are readily accepted and applied in today's world to propel spacecraft into the heavens.

Since the beginning of the space flight program of the United States in 1957, many various unmanned spacecraft have been launched successfully and have ultimately revealed many new horizons that were previously only imagined. With the launch of TIROS 1, the first full-time meteorological satellite, on April 1, 1960, it became quite evident that the satellite and the data generated from it proved

The citations on this and following pages follow the style of the Journal of Applied Meteorology.

worthwhile and exciting when applied to meteorological problems. The TIROS series extended man's understanding of the formation and distribution of various cloud systems and produced data on global cloud cover which provided valuable information on global heat balance and water vapor distribution. Furthermore, the TIROS series provided the meteorologist with almost real time photographs of weather systems and permitted early detection of hurricanes, thereby permitting more accurate forecasts.

As technology rapidly progressed and the meteorological satellite program grew, vast numbers of special applications were investigated. Rainfall estimation was one of these.

2. BACKGROUND

Lethbridge (1967), at Pennsylvania State University, conducted one of the earliest studies comparing local rainfall with image brightness and infrared (IR) temperatures. As technology advanced over the next 6 years and systems for data transmission and acquisition improved, more detailed studies were begun. Pioneers in these efforts were Simpson and Woodley (1971), Sikdar (1972), Martin and Scherer (1973), and Follansbee (1973).

Martin and Scherer (1973) furnish a fairly complete review of methods to estimate rainfall (up to 1973) from either visible (VIS) or IR satellite imagery. Follansbee (1973) primarily deals with rain-producing clouds in his empirical approach to areal daily average rainfall estimations.

More recent applications of rainfall estimation have been conducted by Allison et al. (1974) using NIMBUS 5 electronically scanning microwave radiometer data over oceans; and by Griffith et al. (1976) using Applications Technology Satellite (ATS-3) imagery over southern Florida.

The first rainfall estimation studies that used geosynchronous satellite imagery were conducted by Follansbee and Oliver (1975) and Oliver and Scofield (1976). As a result of those studies, a scheme for point approximation of convective rainfall was developed by Scofield and Oliver (1977) using Geostationary Operational Environmental Satellite (GOES) VIS and enhanced infrared (EIR) imagery. Recently, Scofield (1978a, 1978b) emphasized the practical applications of the GOES-1 VIS

and EIR imagery to detect and estimate rainfall from thunderstorm-produced flash floods by expanding his point approximation scheme to include areal coverage. Since GOES VIS and IR imagery are provided to the user every 30 min during the system's normal operation and can be adjusted to provide data at 5-min intervals during rapid scan operations (Corbell et al., 1976), a careful severe weather (e.g., flash flood) watch can be maintained over vast areal expanses.

The May 1978 issue of the Bulletin of the American Meteorological Society presented a statement of concern by the American Meteorological Society (1978) regarding actions that must be taken to prevent loss of life in flash floods. Their position makes it clear that much more must be learned about rapid convective rainfall if we are to provide an objective input into the decision making process regarding flash flood forecasting and the associated warnings to the public. Mogil et al. (1978) outlined the current flash flood warning program of the National Weather Service and stressed that additional research is necessary in various data-gathering operations, one of these being the development of techniques for rainfall estimation based on satellite data.

At present, the most accurate rainfall measurements are those obtained from a close network of raingages. It is obvious that raingages cannot be placed everywhere, let alone in a sufficiently dense network that would be economically feasible. Rugged mountainous terrain, remote interior areas on continents, and vast ocean areas are other apparent factors limiting such a raingage network. Even over flat terrain, a close network of raingages may not be representative

if the rainfall is from convective activity. Therefore, alternative methods for approximating rainfall must be sought.

The meteorological radar system is well established and receives much attention from forecasters and hydrologists for precipitation estimates. Though it is less accurate than a close network of rain-gages, the radar system is economically feasible, in most cases, and gives a very good quantitative estimate over large areas. However, the weather radar is chiefly limited to land based operations for rainfall estimates. Furthermore, the employment and maintenance of a complex radar system is dependent upon the user's technology and operating capital, thereby limiting its use to the developed nations. Therefore, with the limitations placed on both the rain-gage networks and weather radars, satellite imagery for rainfall prediction appears to be a viable solution to the problem.

Reynolds and Vonder Haar (1973) compared the reflected solar radiation from ATS-3 imagery with cloud heights determined by using radar. Their study showed a correlation of 0.88, which they feel is significant enough to support the argument that the cumulus height and growth may be inferred from geostationary satellites. Studies by Woodley et al. (1972), Griffith and Woodley (1973) and Griffith et al. (1976) substantiate the same premise that the brighter the cloud on visible imagery, the higher the cloud and the heavier the rainfall. This principle--the higher (colder) the clouds, the heavier the rainfall--was the very basis for later work.

Following the GARP (Global Atmospheric Research Program) Atlantic Tropical Experiment (GATE), Griffith et al. (1976) reported on their

findings from ATS-3 imagery to formulate a procedure for approximating rainfall during daylight hours. The ATS-3 data were digitized by use of a densitometer and later calibrated via gage-adjusted 10-cm radar. They suggested that higher resolution data (e.g., digital GOES data) would have improved the accuracy of their results by 20 to 30%. In a recent paper, Griffith et al. (1978) discussed the feasibility of real time flash flood prediction based on the methodology from their GATE investigations. They presented cumulative rainfall results from the Big Thompson storm (July 31 and August 1, 1976) from GOES IR imagery. Although their approach was somewhat imprecise, they feel that such data could be used in near real time. Once again this demonstrates that digital data are superior to the imagery and should be used when available.

Restraints imposed on a scheme for rainfall estimation from digital GOES data by use of an objective technique would be fairly rigorous. First, the satellite data must be "navigated" (rectified) and then reduced to a suitable spatial resolution. Next, the cloud system of the individual cloud must be isolated and tracked so that rainfall amounts can be computed per grid square over a time interval. Some of the latest work has been accomplished by Scofield (1978b), who demonstrates that his methods using GOES VIS and IR imagery can be applied to flash flood problems. The scheme is relatively simple and is not burdened by the problems of navigation and spatial reduction. His method does, however, rely heavily upon the experience level of the individual interpreting the satellite imagery.

The most important, obvious step when handling satellite imagery

is to accurately grid (navigate) the data to provide maximum resolution. Roth (1969) describes an automated technique for the rectification and mapping of meteorological satellite imagery. His method is subjective, biased toward data selection; whereas, Wolf et al. (1972) and Cherne (1974) improved on the technique Roth developed and navigated the satellite imagery while devising a technique to determine cloud motions. They basically relate the location of the satellite in time and space to the actual surface of the earth and then compare the actual surface and the map projection. Cherne (1974) also describes the immense volumes of data that severely tax even automated methods of data processing.

Hawkins (1977) agrees with Cherne and stresses that the large amounts of data place limitations on all aspects of its use. Therefore, data amounts must be reduced as efficiently as possible while retaining maximum resolution. Another way to minimize the vast amounts of data and retain the maximum resolution would be to observe a significantly smaller areal expanse. The GOES imagery system does this by allowing the user to observe a smaller areal expanse without sacrificing resolution.

Isolating and tracking areas of interest could simply be observed from the imagery in a subjective manner (like Scofield and Oliver, 1977) or by an automated, objective process, whereby exceeding a specified threshold value would trigger a signal for a closer weather watch in that sector. Since an experienced analyst in satellite photo interpretation can take a glimpse at a few pictures of some area of the globe and make some summarizing statements packed with

meteorological information, it seems impossible that an objective, automatic technique could handle all the special cases (Hawkins, 1977). Though it seems that a compromise between the objective and subjective analysis methods will be necessary for some time, the potential value of an objective technique for rainfall estimation is great.

In light of the above, it is hoped that this investigation will be another step toward the formulation of an objective technique for rainfall estimation and will become one that would be used as a supplemental tool by meteorologists and hydrologists responsible for flash flood prediction.

3. THE GOES-1 SYSTEM

The main goal of the GOES satellite program is to increase knowledge and understanding of earth's atmosphere and the processes that take place within it by observing the life cycle and motion of synoptic systems, tropical cyclones, severe thunderstorms, and other related atmospheric phenomena. Another objective of the program is to develop a national and international environmental network that can obtain, process, and transmit the GOES data and weather related warnings in real time (McKowan, 1977).

GOES-1 was launched October 16, 1975 and arrived on station December 18, 1975. Its position is 35,800 km above the equator at 75°W. It travels at a speed of about 11,000 km h⁻¹ in the same direction as the earth's rotation on its axis. At this speed and altitude the satellite remains relatively fixed at its position in space with respect to the surface of earth, and is thus termed a geosynchronous satellite. The satellite maintains a spin rate of 100 rpm as its spin axis remains parallel to the earth's polar axis. This enables the spacecraft to maintain a perpendicular orientation to the earth equatorial plane (Corbell et al., 1976).

The visible infrared spin-scan radiometer (VISSR) is capable of day and night mapping of the earth and the clouds in earth's atmosphere because of the satellite's synchronous spin-stabilized geostationary orbit. The VISSR scans from west to east (left to right) in eight identical VIS channels (0.55-0.70 μ m band) and two redundant IR channels (10.5-12.6 μ m band). The VIS and IR data sets are

produced simultaneously (see Fig. 1) and a full disc of earth as viewed by the IR sensor would consist of 1,821 latitude steps (scan lines) with 3,822 points per step. Thus, the IR sensor detects 6,959,862 separate IR picture elements (pixels). The corresponding resolution is 4 n mi by 2 n mi at satellite subpoint. Furthermore, the associated mode A VIS image, taken simultaneously with the IR image, would consist of 14,568 scan lines and have 15,288 points per line. For a full disc of earth that would amount to more than 222 million pixels with a subpoint resolution of $\frac{1}{2}$ n mi by $\frac{1}{2}$ n mi (McKowan, 1977).

At this point, it is noteworthy to pause and consider the enormous amounts of data that are generated by the GOES system, as well as the methods of data retrieval and redistribution. Since a full disc IR image amounts to almost 7 million pixels, it seems fairly obvious that some data reduction and sectorizing must take place to allow for near real time transmission to the Satellite Field Services Stations (SFSS) and the other users. The unprocessed VISSR data are transmitted to the Command and Data Acquisition (CDA) station's 18.3 m antenna, at Wallops Island, Virginia. The CDA station processes the raw data through a synchronizer/data buffer which separates the VIS and IR data. The VIS data are then transmitted back to the satellite, while the lower resolution IR data are processed through computers for analog transmission via 3 kHz telephone lines direct to the Central Data Distribution Facilities (CDDF) at Marlow Heights, Maryland. The VIS data, received from the satellite, are then relayed to the CDDF via a microwave link from the National Environmental

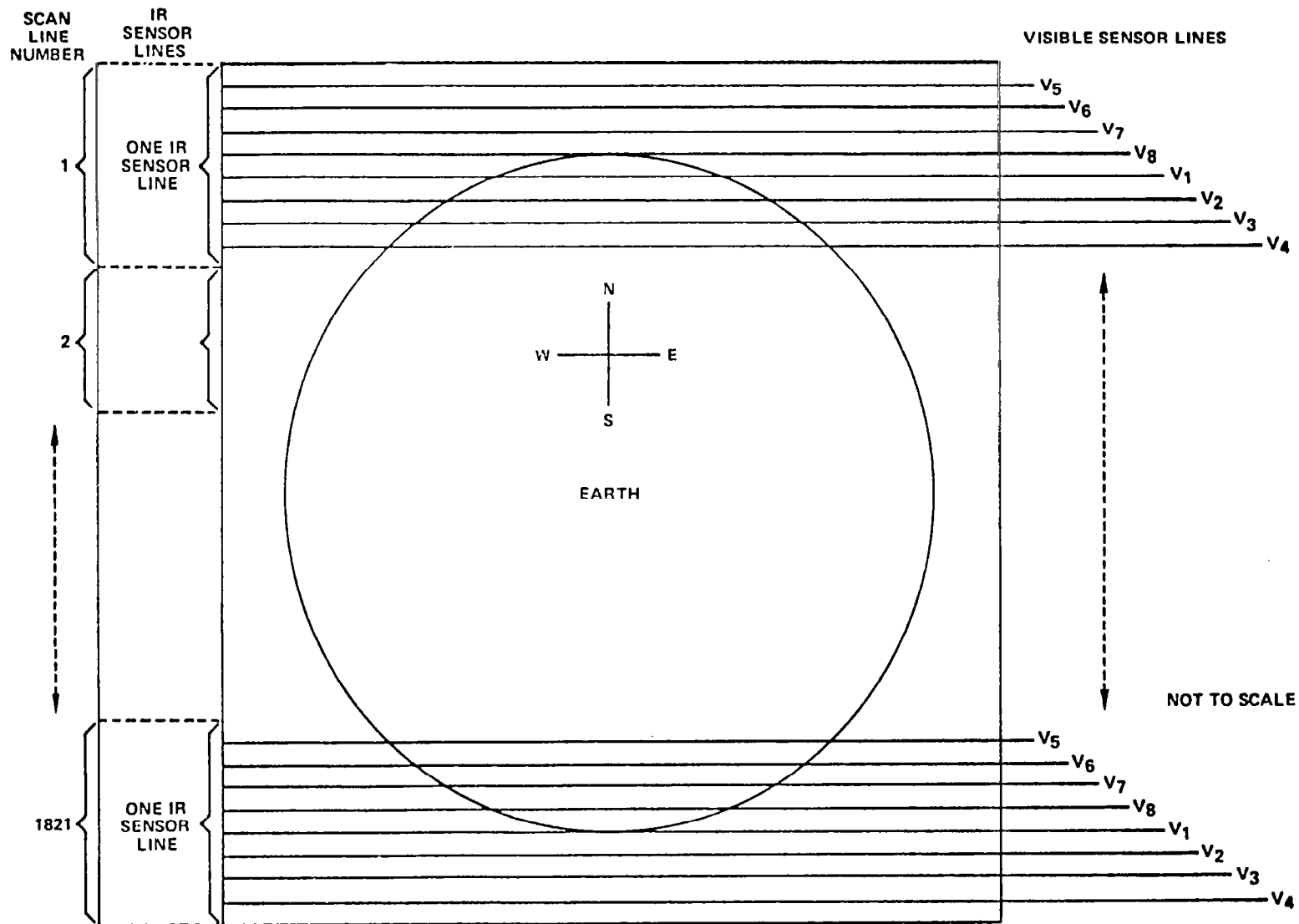


Fig. 1. Assembly of VISSR mode A picture data showing the relationship between infrared and visible sensor lines (from McKowan, 1977).

Satellite Service (NESS) at Suitland, Maryland. The data are then formatted and sectorized by CDDF to allow telephone line transmission to the SFSS's. Fig. 2 illustrates the data flow and depicts the transmission from location to location and the arrival at the SFSS's and the other users. Table 1 represents the locations of SFSS's and their co-located National Weather Service (NWS) units.

Table 1. Current SFSS's in operation (from Corbell et al., 1976).

SFSS	Co-located NWS Units
Washington, D.C.	Washington, D.C. Weather Service Forecast Office (WSFO)
Miami, Florida	National Hurricane Center, Miami
Kansas City, Missouri	National Severe Storms Forecast Center Kansas City, Missouri
San Francisco, California	San Francisco WSFO and Eastern Pacific Hurricane Center
Honolulu, Hawaii	Honolulu WSFO and Central Pacific Hurricane Center
Anchorage, Alaska	Anchorage WSFO, Alaska

The Wallops Island CDA station converts the radiance measurements to equivalent blackbody temperatures (the calibration process). The CDDF sectorizes the digital data and transmits them to the users. The 256 digital count values, assigned during the calibration process, represent specific ranges of temperature. Each count represents a 0.5K change from 330K to 242K and a 1.0K change from 242K to 163K (Fig. 3). Since it is difficult to recognize significant features in IR imagery

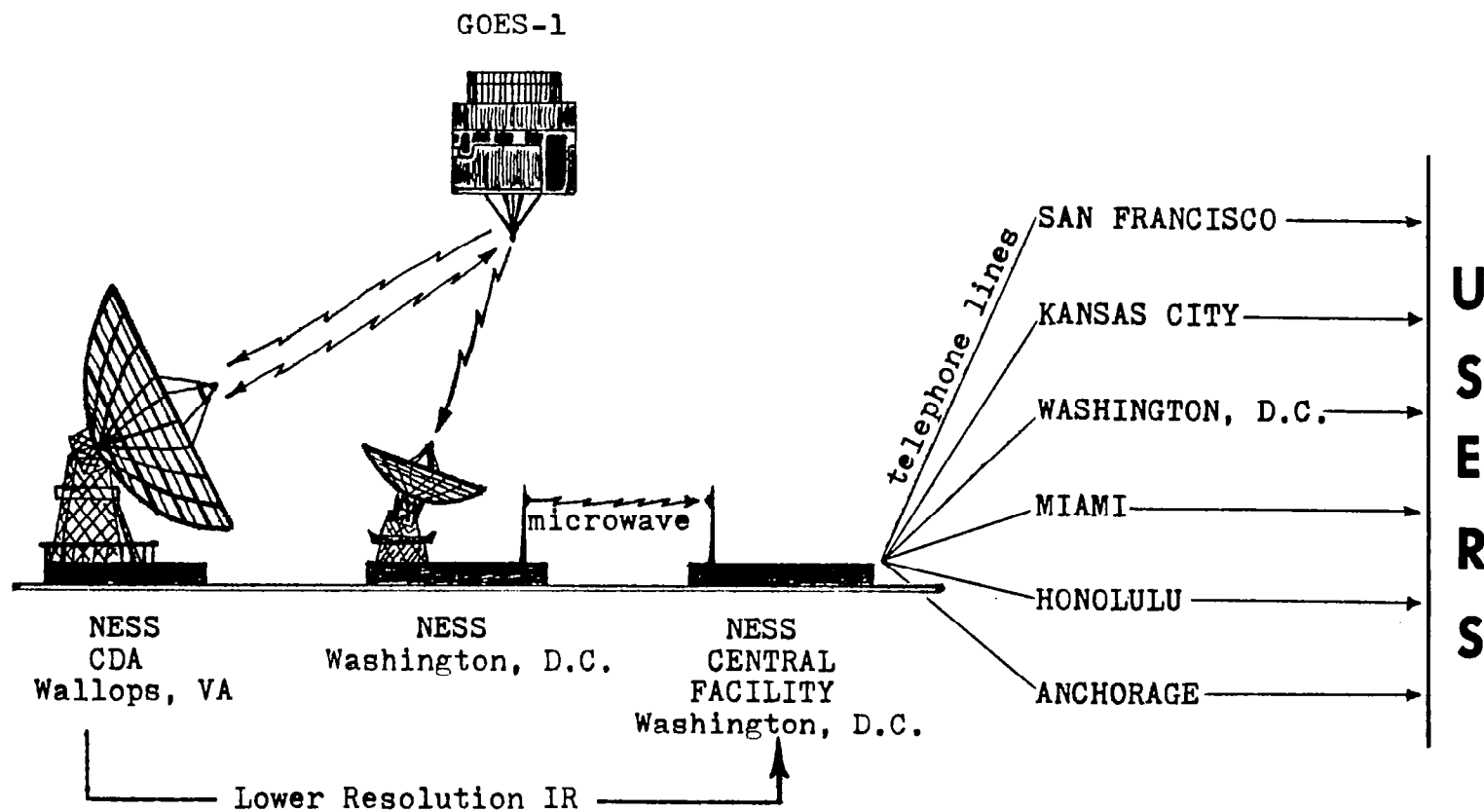


Fig. 2. GOES data flow diagram (after Corbell *et al.*, 1976).

Fig. 3. Standard IR calibration of digital count values to their associated equivalent blackbody temperatures (from Corbell et al., 1976).

COUNT VALUE	KELVIN	CENTIGRADE	FAHRENHEIT	COUNT VALUE	KELVIN	CENTIGRADE	FAHRENHEIT	COUNT VALUE	KELVIN	CENTIGRADE	FAHRENHEIT	COUNT VALUE	KELVIN	CENTIGRADE	FAHRENHEIT	COUNT VALUE	KELVIN	CENTIGRADE	FAHRENHEIT
000	330.0	56.8	134.3	051	304.5	31.3	88.4	102	279.0	5.8	42.5	153	253.5	-19.7	-3.4	204	214.0	-59.2	-74.5
001	329.5	56.3	133.4	052	304.0	30.8	87.5	103	278.5	5.3	41.6	154	253.0	-20.2	-4.3	205	213.0	-60.2	-76.3
002	329.0	55.8	132.5	053	303.5	30.3	86.6	104	278.0	4.8	40.7	155	252.5	-20.7	-5.2	206	212.0	-61.2	-78.1
003	328.5	55.3	131.6	054	303.0	29.8	85.7	105	277.5	4.3	39.8	156	252.0	-21.2	-6.1	207	211.0	-62.2	-79.9
004	328.0	54.8	130.7	055	302.5	29.3	84.8	106	277.0	3.8	38.9	157	251.5	-21.7	-7.0	208	210.0	-63.2	-81.7
005	327.5	54.3	129.8	056	302.0	28.8	83.9	107	276.5	3.3	38.0	158	251.0	-22.2	-7.9	209	209.0	-64.2	-83.5
006	327.0	53.8	128.9	057	301.5	28.3	83.0	108	276.0	2.8	37.1	159	250.5	-22.7	-8.8	210	208.0	-65.2	-85.3
007	326.5	53.3	128.0	058	301.0	27.8	82.1	109	275.5	2.3	36.2	160	250.0	-23.2	-9.7	211	207.0	-66.2	-87.1
008	326.0	52.8	127.1	059	300.5	27.3	81.2	110	275.0	1.8	35.3	161	249.5	-23.7	-10.6	212	206.0	-67.2	-88.9
009	325.5	52.3	126.2	060	300.0	26.8	80.3	111	274.5	1.3	34.4	162	249.0	-24.2	-11.5	213	205.0	-68.2	-90.7
010	325.0	51.8	125.3	061	299.5	26.3	79.4	112	274.0	.8	33.5	163	248.5	-24.7	-12.4	214	204.0	-69.2	-92.5
011	324.5	51.3	124.4	062	299.0	25.8	78.5	113	273.5	.3	32.6	164	248.0	-25.2	-13.3	215	203.0	-70.2	-94.3
012	324.0	50.8	123.5	063	298.5	25.3	77.6	114	273.0	-.2	31.7	165	247.5	-25.7	-14.2	216	202.0	-71.2	-96.1
013	323.5	50.3	122.6	064	298.0	24.8	76.7	115	272.5	-.7	30.8	166	247.0	-26.2	-15.1	217	201.0	-72.2	-97.9
014	323.0	49.8	121.7	065	297.5	24.3	75.8	116	272.0	-1.2	29.9	167	246.5	-26.7	-16.0	218	200.0	-73.2	-99.7
015	322.5	49.3	120.8	066	297.0	23.8	74.9	117	271.5	-1.7	29.0	168	246.0	-27.2	-16.9	219	199.0	-75.2	-101.5
016	322.0	48.8	119.9	067	296.5	23.3	74.0	118	271.0	-2.2	28.1	169	245.5	-27.7	-17.8	220	198.0	-75.2	-103.3
017	321.5	48.3	119.0	068	296.0	22.8	73.1	119	270.5	-2.7	27.2	170	245.0	-28.2	-18.7	221	197.0	-76.2	-105.1
018	321.0	47.8	118.1	069	295.5	22.3	72.2	120	270.0	-3.2	26.3	171	244.5	-28.7	-19.6	222	196.0	-77.2	-106.9
019	320.5	47.3	117.2	070	295.0	21.8	71.3	121	269.5	-3.7	25.4	172	244.0	-29.2	-20.5	223	195.0	-78.2	-108.7
020	320.0	46.8	116.3	071	294.5	21.3	70.4	122	269.0	-4.2	24.5	173	243.5	-29.7	-21.4	224	194.0	-79.2	-110.5
021	319.5	46.3	115.4	072	294.0	20.8	69.5	123	268.5	-4.7	23.6	174	243.0	-30.2	-22.3	225	193.0	-80.2	-112.3
022	319.0	45.8	114.5	073	293.5	20.3	68.6	124	268.0	-5.2	22.7	175	242.5	-30.7	-23.2	226	192.0	-81.2	-114.1
023	318.5	45.3	113.6	074	293.0	19.8	67.7	125	267.5	-5.7	21.8	176	242.0	-31.2	-24.1	227	191.0	-82.2	-115.9
024	318.0	44.8	112.7	075	292.5	19.3	66.8	126	267.0	-6.2	20.9	177	241.0	-31.7	-25.0	228	190.0	-83.2	-117.7
025	317.5	44.3	111.8	076	292.0	18.8	65.9	127	266.5	-6.7	20.0	178	240.0	-32.2	-25.9	229	189.0	-84.2	-119.5
026	317.0	43.8	110.9	077	291.5	18.3	65.0	128	266.0	-7.2	19.1	179	239.0	-32.7	-26.8	230	188.0	-85.2	-121.3
027	316.5	43.3	110.0	078	291.0	17.8	64.1	129	265.5	-7.7	18.2	180	238.0	-33.2	-27.7	231	187.0	-86.2	-123.1
028	316.0	42.8	109.1	079	290.5	17.3	63.2	130	265.0	-8.2	17.3	181	237.0	-33.7	-28.6	232	186.0	-87.2	-124.9
029	315.5	42.3	108.2	080	290.0	16.8	62.3	131	264.5	-8.7	16.4	182	236.0	-34.2	-29.5	233	185.0	-88.2	-126.7
030	315.0	41.8	107.3	081	289.5	16.3	61.4	132	264.0	-9.2	15.5	183	235.0	-34.7	-30.4	234	184.0	-89.2	-128.5
031	314.5	41.3	106.4	082	289.0	15.8	60.5	133	263.5	-9.7	14.6	184	234.0	-35.2	-31.3	235	183.0	-90.2	-130.3
032	314.0	40.8	105.5	083	288.5	15.3	59.6	134	263.0	-10.2	13.7	185	233.0	-35.7	-32.2	236	182.0	-91.2	-132.1
033	313.5	40.3	104.6	084	288.0	14.8	58.7	135	262.5	-10.7	12.8	186	232.0	-36.2	-33.1	237	181.0	-92.2	-133.9
034	313.0	39.8	103.7	085	287.5	14.3	57.8	136	262.0	-11.2	11.9	187	231.0	-36.7	-34.0	238	180.0	-93.2	-135.7
035	312.5	39.3	102.8	086	287.0	13.8	56.9	137	261.5	-11.7	11.0	188	230.0	-37.2	-34.9	239	179.0	-94.2	-137.5
036	312.0	38.8	101.9	087	286.5	13.3	56.0	138	261.0	-12.2	10.1	189	229.0	-37.7	-35.8	240	178.0	-95.2	-139.3
037	311.5	38.3	101.0	088	286.0	12.8	55.1	139	260.5	-12.7	9.2	190	228.0	-38.2	-36.7	241	177.0	-96.2	-141.1
038	311.0	37.8	100.1	089	285.5	12.3	54.2	140	260.0	-13.2	8.3	191	227.0	-38.7	-37.6	242	176.0	-97.2	-142.9
039	310.5	37.3	99.2	090	285.0	11.8	53.3	141	259.5	-13.7	7.4	192	226.0	-39.2	-38.5	243	175.0	-98.2	-144.7
040	310.0	36.8	98.3	091	284.5	11.3	52.4	142	259.0	-14.2	6.5	193	225.0	-39.7	-39.4	244	174.0	-99.2	-146.5
041	309.5	36.3	97.4	092	284.0	10.8	51.5	143	258.5	-14.7	5.6	194	224.0	-40.2	-40.3	245	173.0	-100.2	-148.3
042	309.0	35.8	96.5	093	283.5	10.3	50.6	144	258.0	-15.2	4.7	195	223.0	-40.7	-41.2	246	172.0	-101.2	-150.1
043	308.5	35.3	95.6	094	283.0	9.8	49.7	145	257.5	-15.7	3.8	196	222.0	-41.2	-42.1	247	171.0	-102.2	-151.9
044	308.0	34.8	94.7	095	282.5	9.3	48.8	146	257.0	-16.2	2.9	197	221.0	-41.7	-43.0	248	170.0	-103.2	-153.7
045	307.5	34.3	93.8	096	282.0	8.8	47.9	147	256.5	-16.7	2.0	198	220.0	-42.2	-43.9	249	169.0	-104.2	-155.5
046	307.0	33.8	92.9	097	281.5	8.3	47.0	148	256.0	-17.2	1.1	199	219.0	-42.7	-44.8	250	168.0	-105.2	-157.3
047	306.5	33.3	92.0	098	281.0	7.8	46.1	149	255.5	-17.7	.2	200	218.0	-43.2	-45.7	251	167.0	-106.2	-159.1
048	306.0	32.8	91.1	099	280.5	7.3	45.2	150	255.0	-18.2	-.7	201	217.0	-43.7	-46.6	252	166.0	-107.2	-160.9
049	305.5	32.3	90.2	100	280.0	6.8	44.3	151	254.5	-18.7	-1.6	202	216.0	-44.2	-47.5	253	165.0	-108.2	-162.7
050	305.0	31.8	89.3	101	279.5	6.3	43.4	152	254.0	-19.2	-2.5	203	215.0	-44.7	-48.4	254	164.0	-109.2	-164.5
																255	163.0	-110.2	-166.3

when temperature gradients are small, enhancement's main purpose is to provide contrast between fog and haze, thunderstorm tops, ocean current boundaries, and terrain features. The enhancement curves that are utilized with IR imagery furnish field forecasters with another tool by which an improved weather forecast, watch, and/or warning can be disseminated to the public. The assorted enhancement curves available to SFSS's are outlined by Corbell et al. (1976).

The enhancement curve that receives the most attention for convective precipitation estimation is the M_B curve because it allows better definition of very cold domes (Fig. 4). One of the drawbacks, however, is that specific temperatures below -65°C cannot be obtained from the IR imagery. It does, however, progress from black to white gradually rather than producing a complete white-out at temperatures colder than -65°C . This provides the user with a good idea just where the coldest tops are and consequently locates the areas of maximum precipitation.

Scofield and Oliver (1977) have used the M_B curve as a basis for their rainfall estimation studies. This investigation uses the concept of enhancement as the foundation for this investigation.

Inasmuch as this research primarily deals with digital GOES data, further discussion will be limited to details related to this investigation. Information concerning subsystems of the spacecraft, archival of the data, and other details can be found in Corbell et al. (1976) or McKowan (1977).

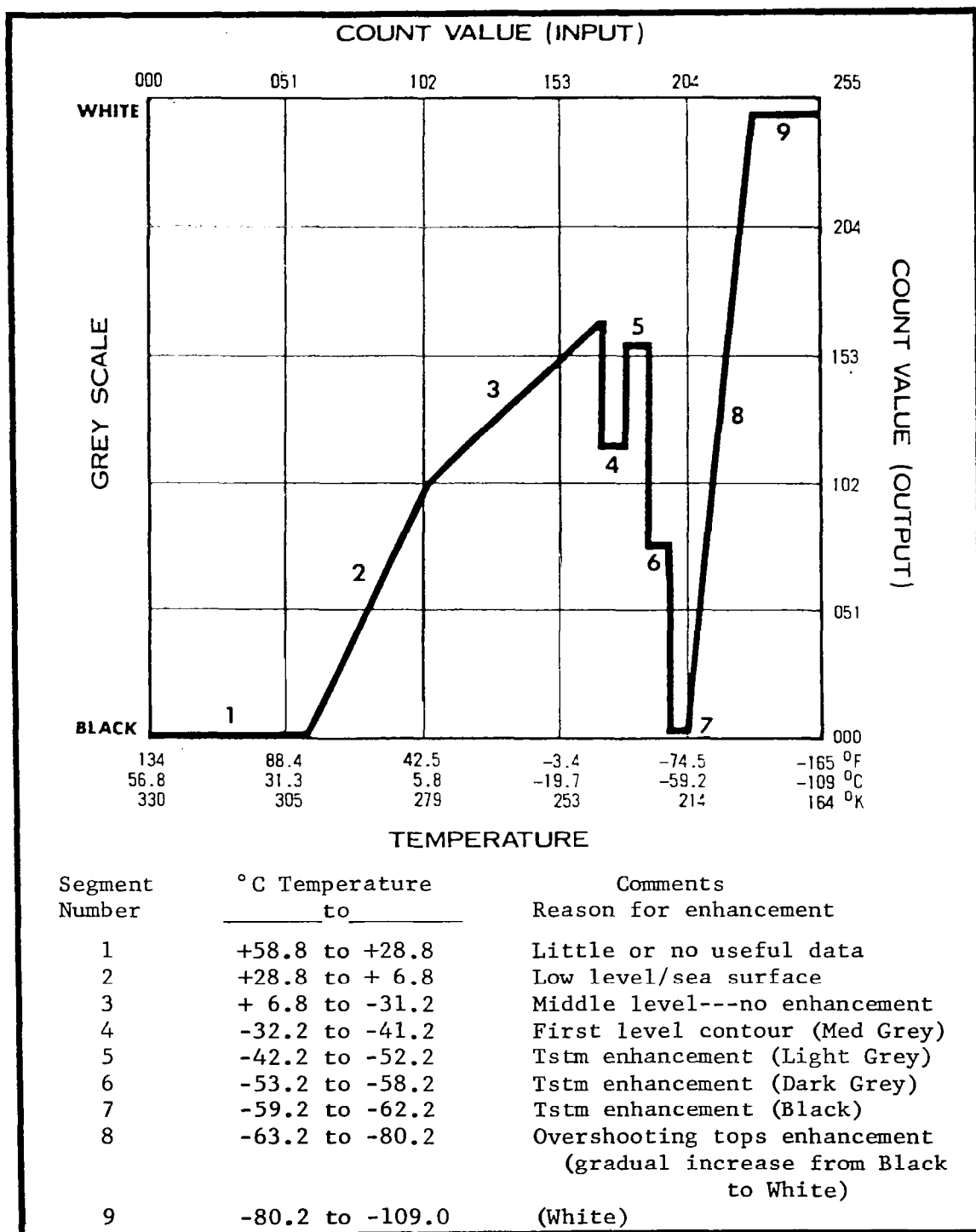


Fig. 4. M_B enhancement curve (after Corbell et al., 1976).

4. DATA

In order to examine the feasibility of a convective rainfall approximation scheme from digital GOES-1 data, two primary data bases are required, as well as some supplemental, supportive data. First, it is necessary to construct a ground truth for comparisons with the satellite rainfall estimations. For this part of the study, data from the National Climatic Center (NCC) publications for May 1978 were used in order to determine raingage precipitation amounts for the 24-h and hourly time segments. Second, and most important, the digital GOES-1 data were obtained from the Man Computer Interactive Data Access System (McIDAS) at the University of Wisconsin. McIDAS receives the satellite data directly from the raw GOES data base.

a. Raingage Data

The NCC data were carefully extracted from the May 1978 publications. Climatological Data (Vol. 83, No. 5) contains the 24-h precipitation amounts for stations in the 480 km by 480 km square centered on College Station (CLL), Texas. The Hourly Precipitation Data (Vol. 28, No. 5) contains rainfall rates for the hourly time intervals of interest. National Weather Service radar summaries and Texas A&M University (TAMU) digital radar information supplemented the analysis of the raingage amounts by enabling a fairly accurate positioning of precipitation areas versus precipitation-free areas. The two forms of radar data indicated speed and direction of movement of the system and individual cells, as well as a clarification of rain intensity and location.

b. Digital GOES-1 Data

As mentioned earlier, a single satellite image consists of millions of bytes of information, and the data must be handled carefully to reduce them to specific areas of interest while maintaining maximum resolution. The McIDAS data used in this investigation were produced with VIS mode data of 1 km by 1 km resolution and IR mode data with 4 km by 4 km resolution. The VIS data were not used because the night terminator moved across the study area during the first hour of investigation and rendered the data of little value for rainfall estimations due to lack of visible light. An investigation of VIS data during the daytime hours would be valuable because the VIS data have superior resolution that would allow even better rain gauge and radar comparisons.

The IR data, which provide nearly continuous viewing of earth, have 4 km resolution by virtue of the method with which the McIDAS handles the data. Whereas, the GOES system records an IR pixel in a 4 km (horizontally) by 8 km (vertically) resolution (McKowan, 1977), the McIDAS simply divides the pixel into two 4 km by 4 km pixels and displays them over two adjacent sensor lines (Young, 1978). The resolution, therefore, is implied as 4 km, but in reality it is not because the VISSR integrates the signal over the 8 km interval. However, for data handling, the 4 km pixel appears to be in a less confusing and more usable form.

The GOES data were extracted from the nine-track McIDAS tapes by using a computer programming technique developed by Henderson (1979).

c. Supplemental Data

Supportive data for this investigation were gathered from several different areas. The TAMU digital weather radar provided data for the same time frame as this study. The VIL (vertical integration of liquid water content) maps, produced by McAnelly (1979), were used to fine tune the raingage analysis, and then later were compared to the digital GOES-1 data. The rawinsonde and some synoptic data that were used in this investigation came from NASA's AVE VII (Atmospheric Variability Experiment) experiment¹ (Davis et al., 1978). The remainder of the NWS synoptic data, as well as GOES-1 images, Weather Wire, and Service "C" teletype data were gathered from the TAMU Department of Meteorology archive.

1. Atmospheric Sciences Division, Space Sciences Laboratory, NASA Marshall Space Flight Center, Alabama 35812

5. RESULTS

This investigation was conducted over the region of Texas depicted by Fig. 5. College Station (TAMU) is positioned in the center of the two concentric boxes. The large box is 480 km by 480 km, and the smaller box is 240 km by 240 km. The raingage analyses were performed over the larger box to ensure continuity, but will be presented here only for the smaller box to allow maximum resolution for the comparisons with the digital GOES-1 data. The GOES data were analyzed for rainfall within the 240 km by 240 km box.

a. The Synoptic Situation

At 1820 CDT (2320 GMT) on Tuesday, May 2, 1978, the National Severe Storm Forecast Center at Kansas City issued Tornado Watch Number 97 for portions of central and southeastern Texas and adjacent coastal waters. The watch, valid from 1900 CDT until 0100 CDT (0000-0600 GMT), was issued because a strong upper level low was tracking across the south central United States and triggering severe thunderstorms and associated phenomena as it moved slowly eastward above a somewhat stationary frontal system (Fig. 6a). The warm front stretched across Texas from Del Rio to San Antonio to Houston and on eastward toward Louisiana. This sluggishly moving frontal system and the excess moisture that was stacked from low to mid levels in the troposphere, would continue to interact with the upper level flow (Fig. 6b), and thus maintain the potentially severe weather pattern.

As the upper level low moved eastward, numerous warnings of

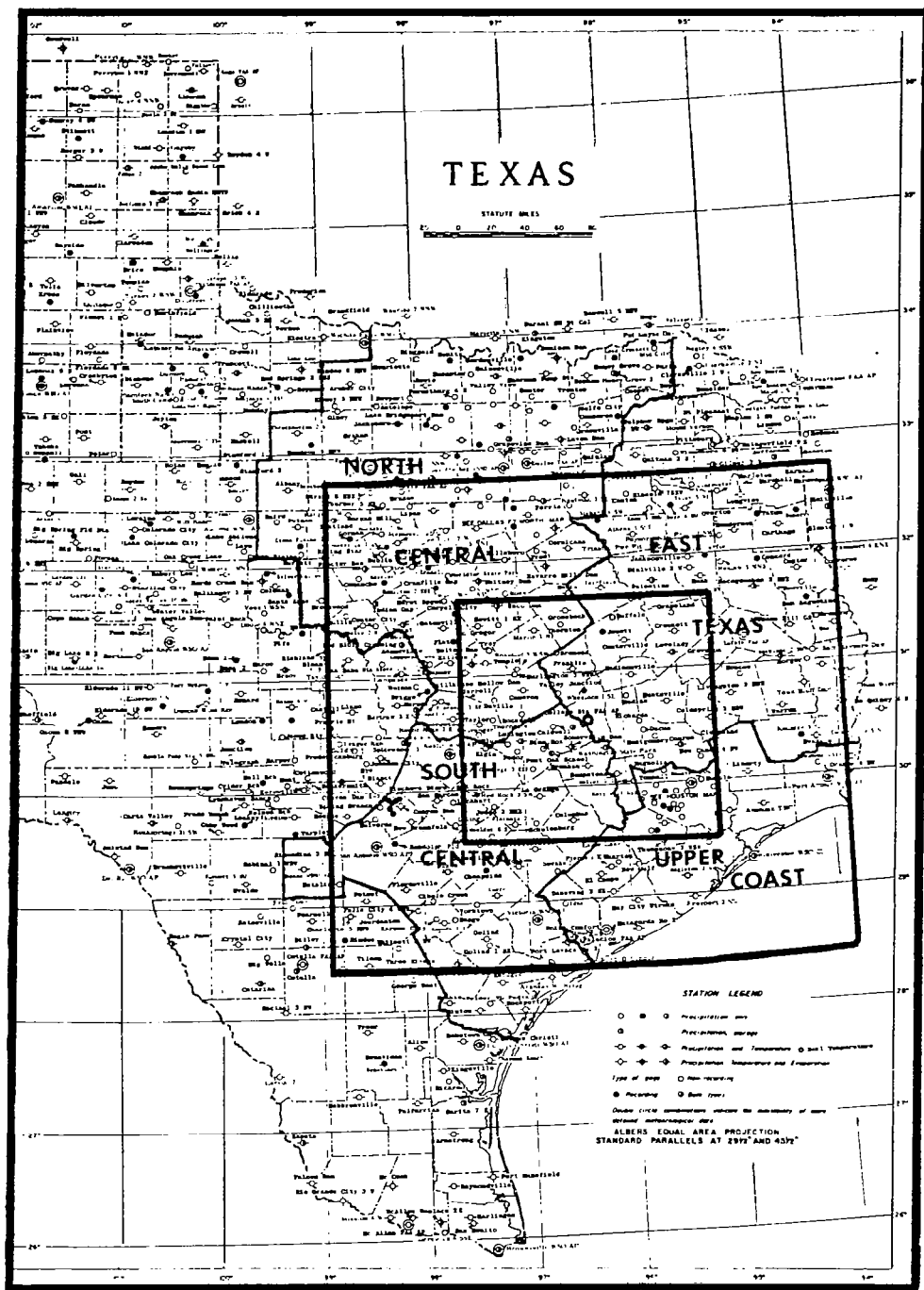


Fig. 5. Area under investigation (small box is 240 km by 240 km and the larger box is 480 km by 480 km) with CLL located at the center.

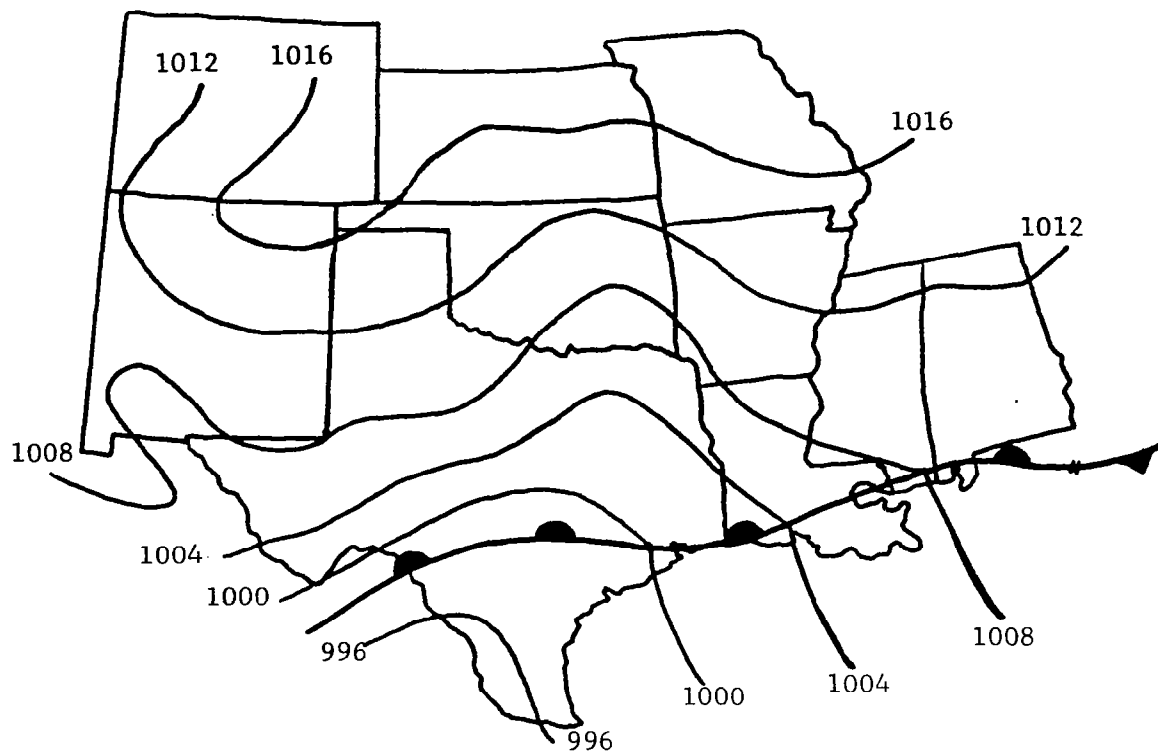


Fig. 6a. NWS surface analysis at 0000 GMT, May 3, 1978.

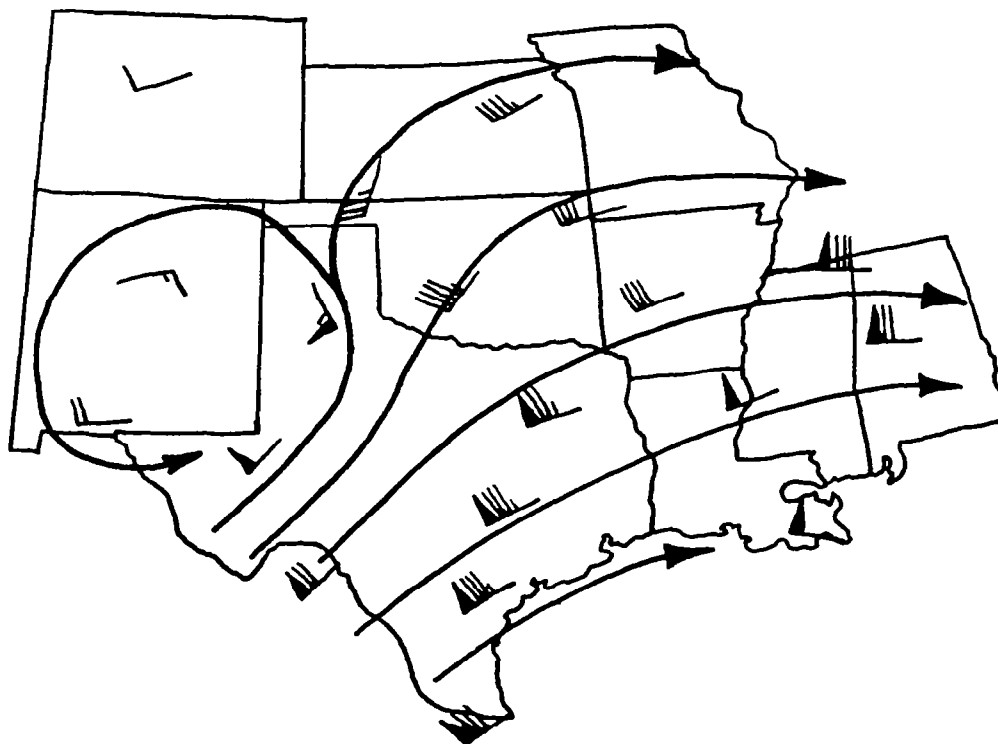


Fig. 6b. 300 mb upper level wind at 0000 GMT, May 3, 1978.

severe thunderstorms were issued by regional NWS Offices (NWSO) via the weather wire. A severe weather statement issued by the NWSO at Houston at 2005 CDT (0105 GMT) noted that the tornado watch was still in effect for most of southeast Texas and that the thunderstorm activity nearest to East Texas was just west of Somerville Dam. The heaviest thunderstorm activity occurring at 2035 CDT (0135 GMT) was in the vicinity of the line echo wave pattern (LEWP) located in South Central Texas, as illustrated by Fig. 7. The NWS reported rains in excess of 50 mm h^{-1} from those storms in and near the LEWP and further reported that all precipitation was moving to the east at 13 m s^{-1} .

At 2115 CDT (0215 GMT) the NWSO at San Antonio issued a flash flood watch for the remainder of the night for the area along and east of a line from Corpus Christi to Victoria to College Station. The forecasters believed that the heavy thunderstorm line (LEWP) moving into that region would produce rains in excess of 50 mm with the potential for some localized rainfall amounting to near 125 mm. By 2135 CDT (0235 GMT), the NWS reported a line of heavy thunderstorms, 24 km wide, just west of College Station (Fig. 8). This line extended southward into South Central Texas and was reportedly moving to the southeast at 13 m s^{-1} . Other thundershowers and isolated heavy thunderstorms were observed 40 km northeast of College Station and also in the area of Lakes Conroe and Livingston. At 2230 CDT (0330 GMT), however, the NWSO at Austin cancelled the tornado and flash flood watches for much of central Texas because the heaviest activity had moved into East Texas where the tornado and flash flood watches still remained in effect.

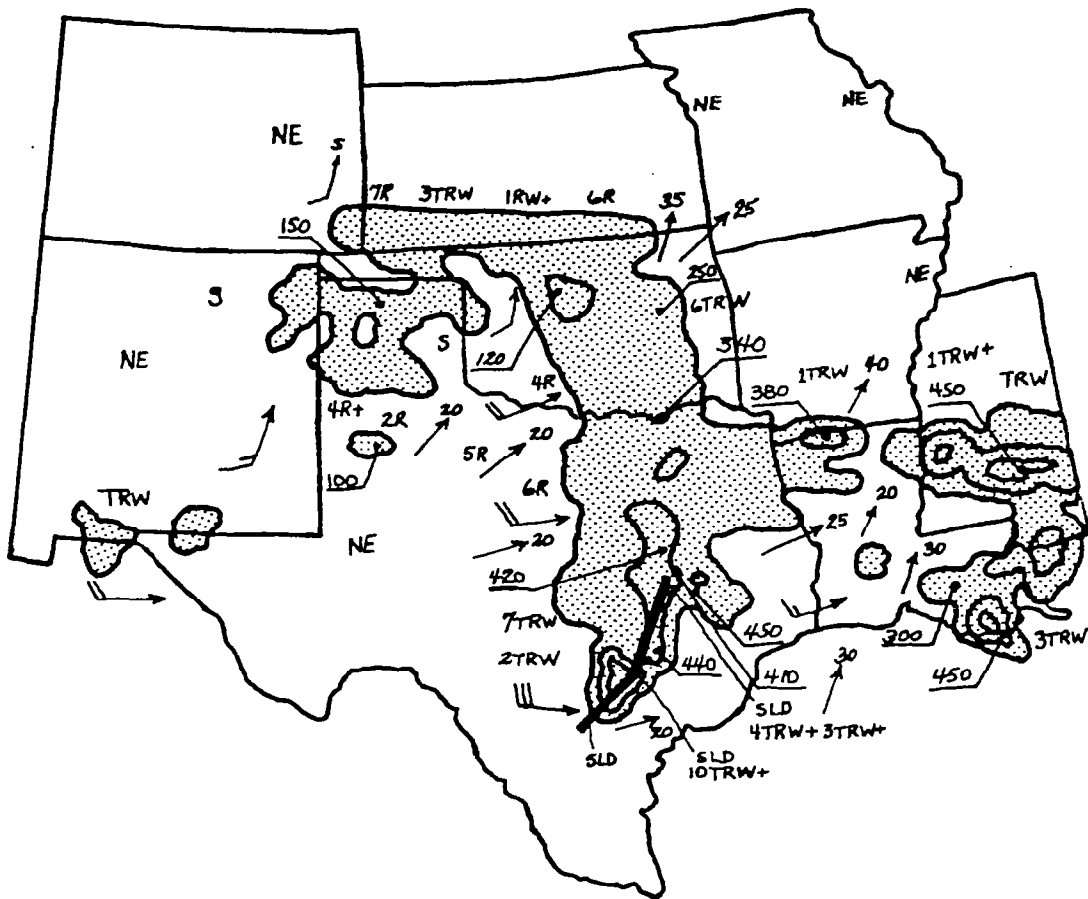


Fig. 8. NWS radar summary at 0235 GMT, May 3, 1978.

As the evening progressed the thunderstorm activity pressed further eastward and began to dissipate rapidly while leaving only scattered thunderstorms across eastern Texas and the upper coastal areas. At 0145 CDT (0645 GMT), Wednesday, May 3, 1978, the NWS cancelled all the watches in Texas because the system had decreased sufficiently in both areal coverage and intensity, and no longer posed a threat for heavy rain or flash flooding.

b. The Raingage Analysis

Careful analyses were performed on the reported raingage amounts collected on the evening of May 2, 1978, across central and eastern Texas. These are presented over the next few pages. Fig. 9 represents the 24-h (02/1200 GMT - 03/1200 GMT) rainfall analysis for the area of investigation within the 240 km by 240 km box centered on TAMU (CLL). Although this portion of the investigation closely examines a 3-h segment (0100-0400 GMT) within the 24-h period, it is noteworthy to point out that much of the precipitation fell within a 3- to 5-h period, and in one instance within 1-h. Table 2 depicts the amounts of rainfall reported and the associated time intervals within which precipitation occurred.

To ensure continuity with the 24-h data, each hourly segment of precipitation was analyzed over the 480 km by 480 km box and then presented here on the smaller, 240 km by 240 km box. A technique using the NWS radar summaries, TAMU's digital radar data, NCC's hourly precipitation data, graphical addition and subtraction of isohyet fields of rainfall, and the author's 15 years of observing and

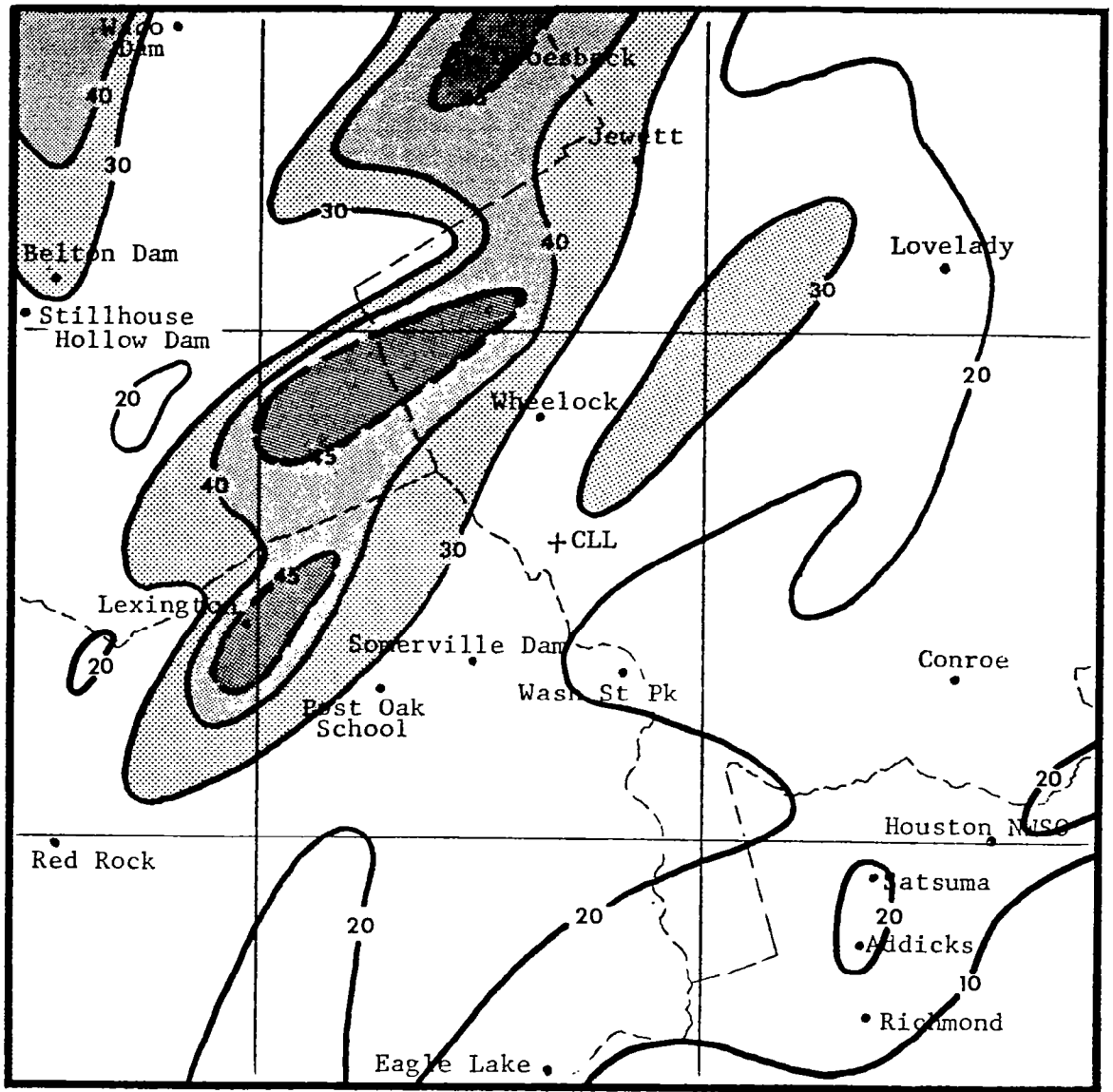


Fig. 9. 24-h rainfall analysis (02/1200 GMT - 03/1200 GMT) in mm for a 240 km by 240 km box centered on CLL.

Table 2. Hourly rainfall amounts and 3-h/24-h total rainfall in mm.

Location	First hour	Second hour	Third hour	3-h total	24-h total
Belton Dam	4	7	0	11	38
Conroe	0	0	0	0	10
Eagle Lake	0	0	5	5	10
Groesbeck	3	36	5	44	48
Houston-WSMO	0	3	0	3	10
Houston-Addicks	1	1	13	15	21
Houston-Satsuma	0	1	0	1	20
Jewett	0	8	16	24	28
Lexington	3	33	5	41	48
Lovelady	0	0	14	14	21
Post Oak School	2	1	17	20	26
Red Rock	0	20	0	20	25
Richmond	0	1	4	5	16
Somerville Dam	3	0	13	16	20
Stillhouse Hollow Dam	4	4	0	8	25
Waco Dam	12	4	1	17	25
Washington State Park	0	3	8	11	18
Wheelock	4	11	3	18	20

forecasting experience was used to analyze Figs. 10-13. Figs. 10, 11, and 12 represent each hour of rainfall, whereas, Fig. 13 is the total rainfall for the 3-h interval.

c. The Satellite Analysis

The digital GOES-1 data were recovered from nine-track McIDAS tapes by using a computer programming technique by Henderson (1979) and subsequently made available for this rainfall estimation study. The navigated, digital count values are plotted on a 76 cm by 76 cm grid that is representative of the 240 km by 240 km box centered on TAMU. The satellite data obtained from McIDAS contained information for each 15 min interval from 03/0015 GMT until 03/0345 GMT for a total of 15 digital count value maps (DCVM). The first two maps were omitted since little activity of significance was occurring. The remaining 13 DCVMs were used in this study and are presented for comparison with the images based on the M_B enhancement curve (M_B EIR) for 0100, 0200, 0230, 0300, and 0400 GMT over the next few pages.

Naturally, digital counts ran from low (63) to high (222) count values over the computer gridded output maps. However, to make analysis less confusing and to enable simplified presentation of the data, only selected isopleths of the digital counts are shown. Furthermore, since the digital count values provide little meaning as to temperature without a conversion method, Fig. 3 (p. 15) was provided to relate the digital count value to its equivalent blackbody temperature.

The first step before beginning any satellite-derived rainfall

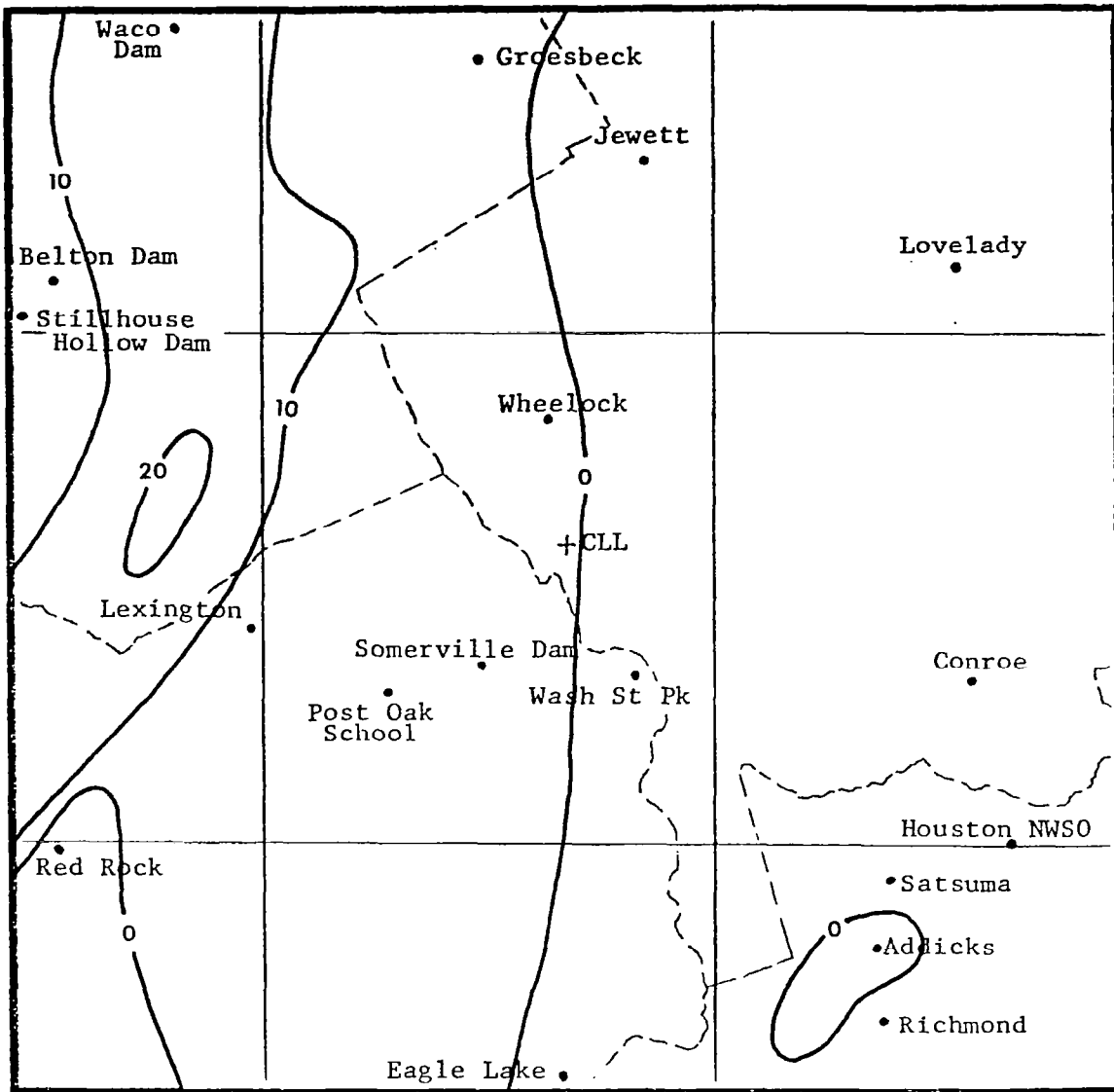


Fig. 10. First hour (0100-0200 GMT) rainfall analysis in mm.

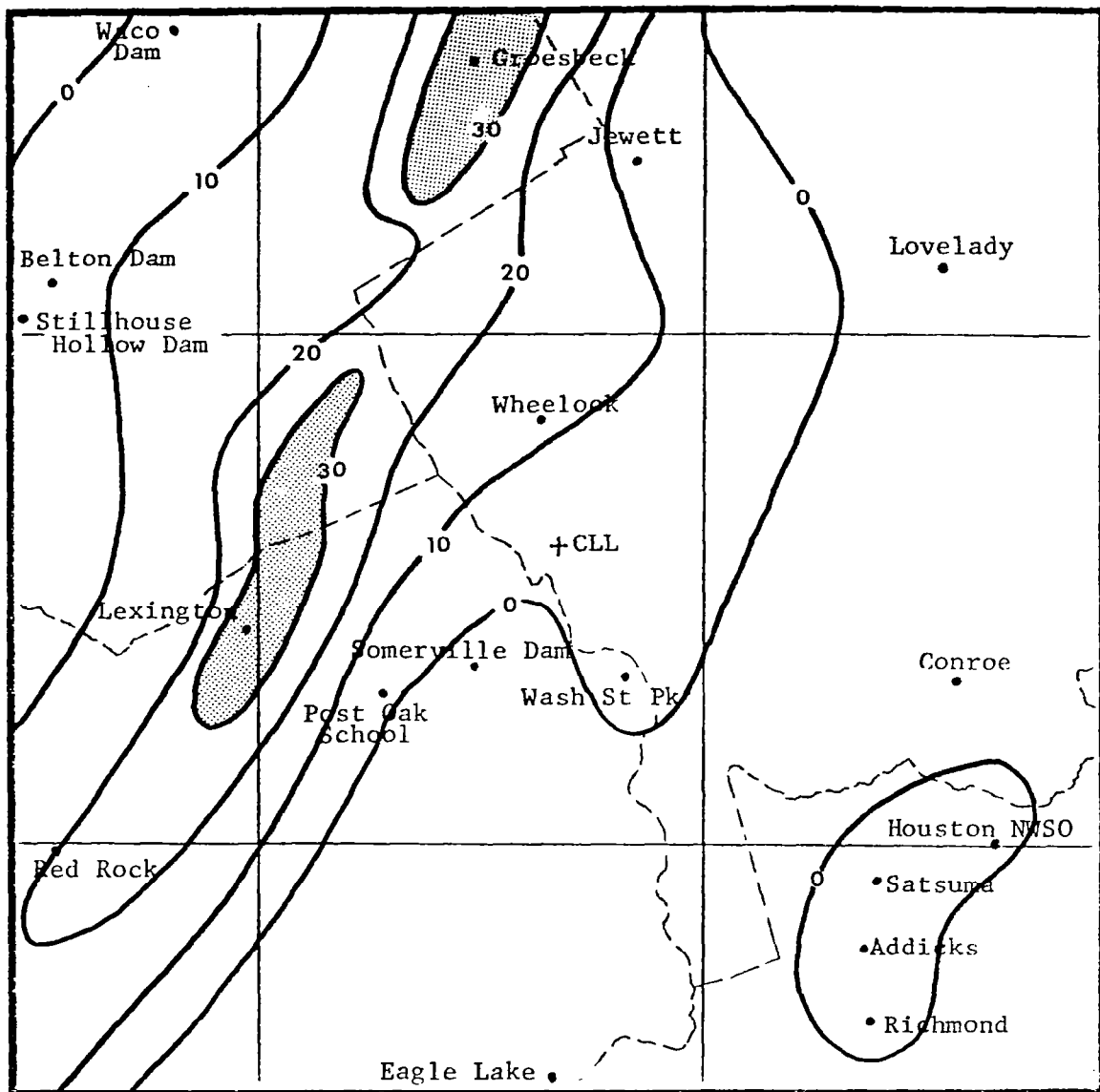


Fig. 11. Second hour (0200-0300 GMT) rainfall analysis in mm.

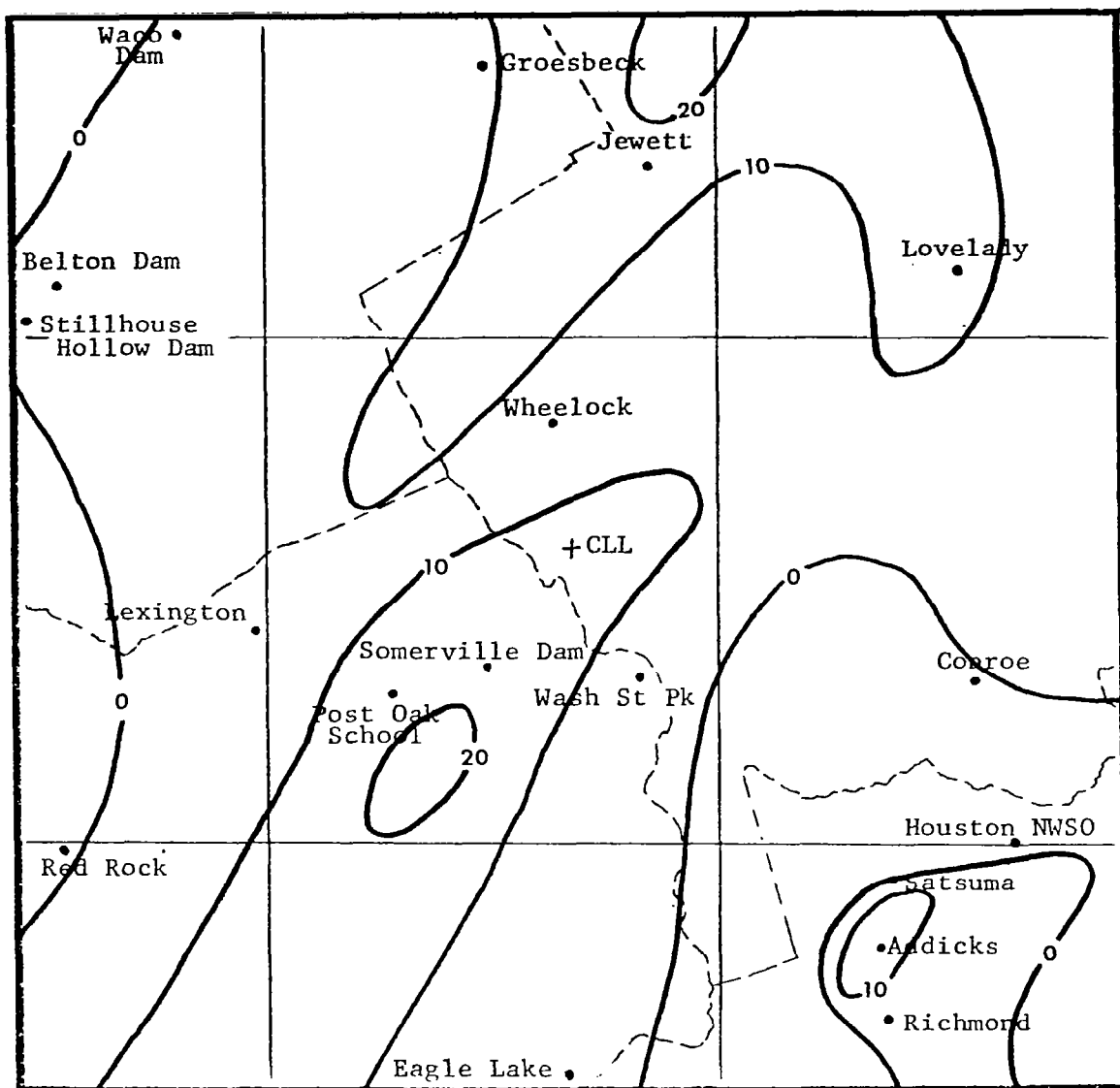


Fig. 12. Third hour (0300-0400 GMT) rainfall analysis in mm.

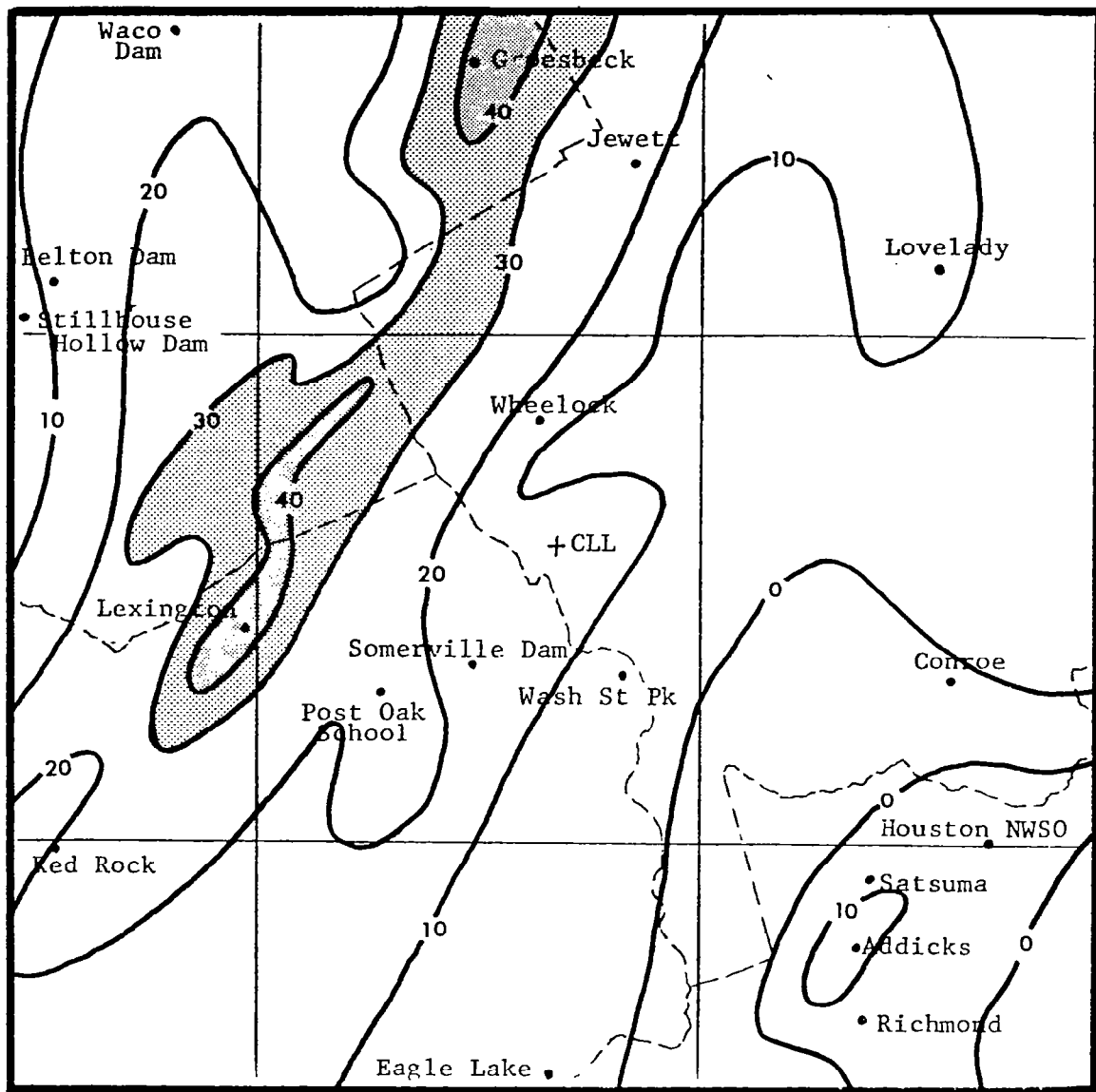


Fig. 13. 3-h (0100-0400 GMT) total rainfall in mm.

approximations was to draw isopleths of the digital count values. After that, a digital count/observed rainfall table was constructed to better understand the variations of digital count values to rainfall amounts. To remain as objective as possible during this stage of the research, only rainfall reporting stations within the study area and under convective activity were used. Table 3 illustrates a portion of the original table prepared for the second hour in the northwest quadrant of study. The given quarter-hour digital count for each

Table 3. Digital count/observed rainfall₁ for the northwest quadrant during the second hour (rainfall in mm h⁻¹).

Time (GMT)	Waco Dam	Groesbeck	Belton Dam	Stillhouse Hollow Dam	Wheelock
0200	215	212	211	211	209
0215	211	215	211	211	211
0230	217	219	218	217	219
0245	209	217	209	210	214
0300	206	214	208	199	215
Rainfall	4	36	7	4	11

station in question was recorded. Then the variation of digital counts was empirically compared to actual precipitation amounts observed. By experimenting with the digital counts and observed rainfall amounts, various count values were tested to determine the best thresholds for rainfall estimates. The digital count 208 proved to give the best estimates when compared with observed cases. Therefore, this study

is based primarily on 208 and higher digital count values.

Of particular interest is the fact that the 208 count value is the overshooting tops enhancement (segment 8) of the M_B enhancement curve shown earlier in Fig. 4 (p. 17). That portion of the M_B curve gradually increases from black (count 208) to white (count 225) and only the very coldest tops are easily seen on the imagery. This will be illustrated further when the 0230 GMT imagery and the DCVM are compared. Furthermore, the availability of digital count values rather than an image threshold appears to indicate that they are important to consider and may very well be the most accurate means to adjust, and thus improve the operational forecast for rainfall amounts in select topographic regions. The conclusions section will discuss this concept further.

Fig. 14 for the 3rd of May at 0045 GMT, depicts the first overshooting tops (count 208-225) moving into the area of study. The 0100 GMT GOES-1 M_B EIR image was reproduced and is presented in Fig. 15. The extent of the storm and the fact that the high, cold cloud tops are widespread should be noted. As the system pushed further eastward (Figs. 16a-d) and the line of thunderstorms moved into the western part of the area, the first of the highest digital counts (220-222) was observed (Fig. 16d). Fig. 17, the 0200 GMT satellite image, shows the area where the highest digital counts (coldest temperatures) were observed. They do not, however, provide information that would be usable for high resolution precipitation evaluations. The DCVMs for the next hour (Figs. 18a&b; 20a&b) are the most interesting and revealing in this investigation. The 0200 GMT and

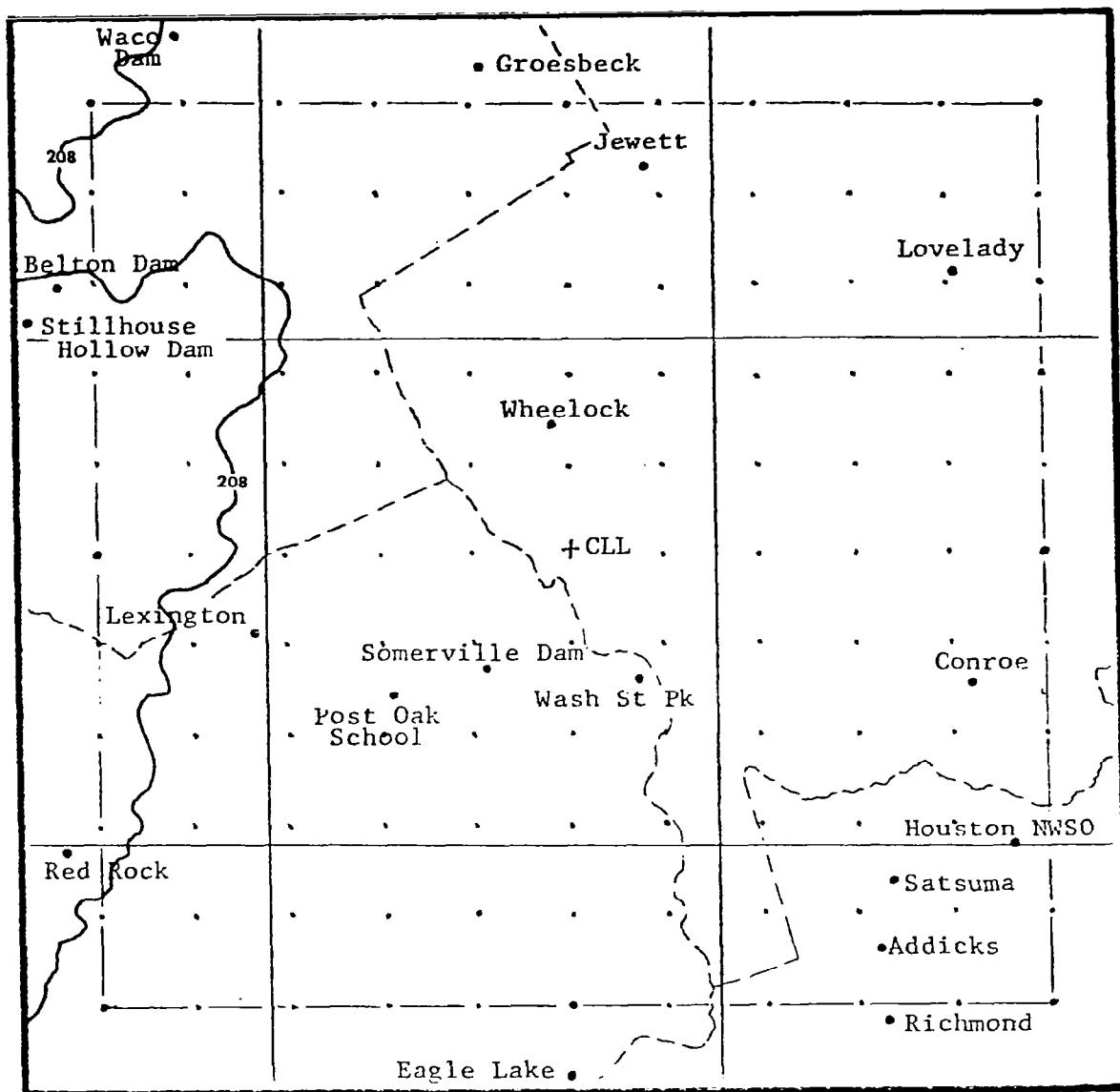


Fig. 14. Digital count value map (DCVM) at 03/0045 GMT.



Fig. 15. 0100 GMT GOES-1 M_B EIR image.

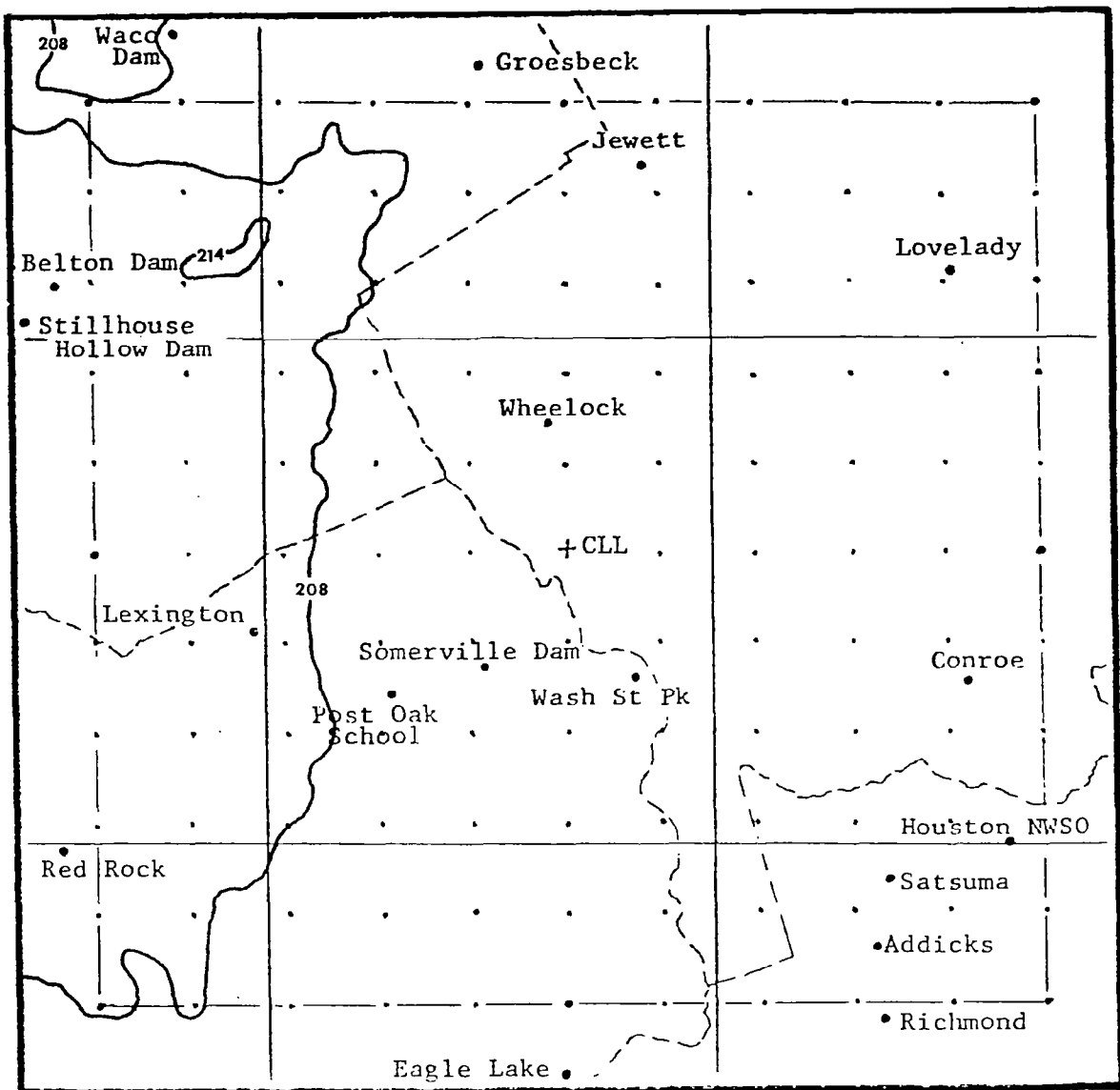


Fig. 16a. DCVM at 03/0100 GMT.

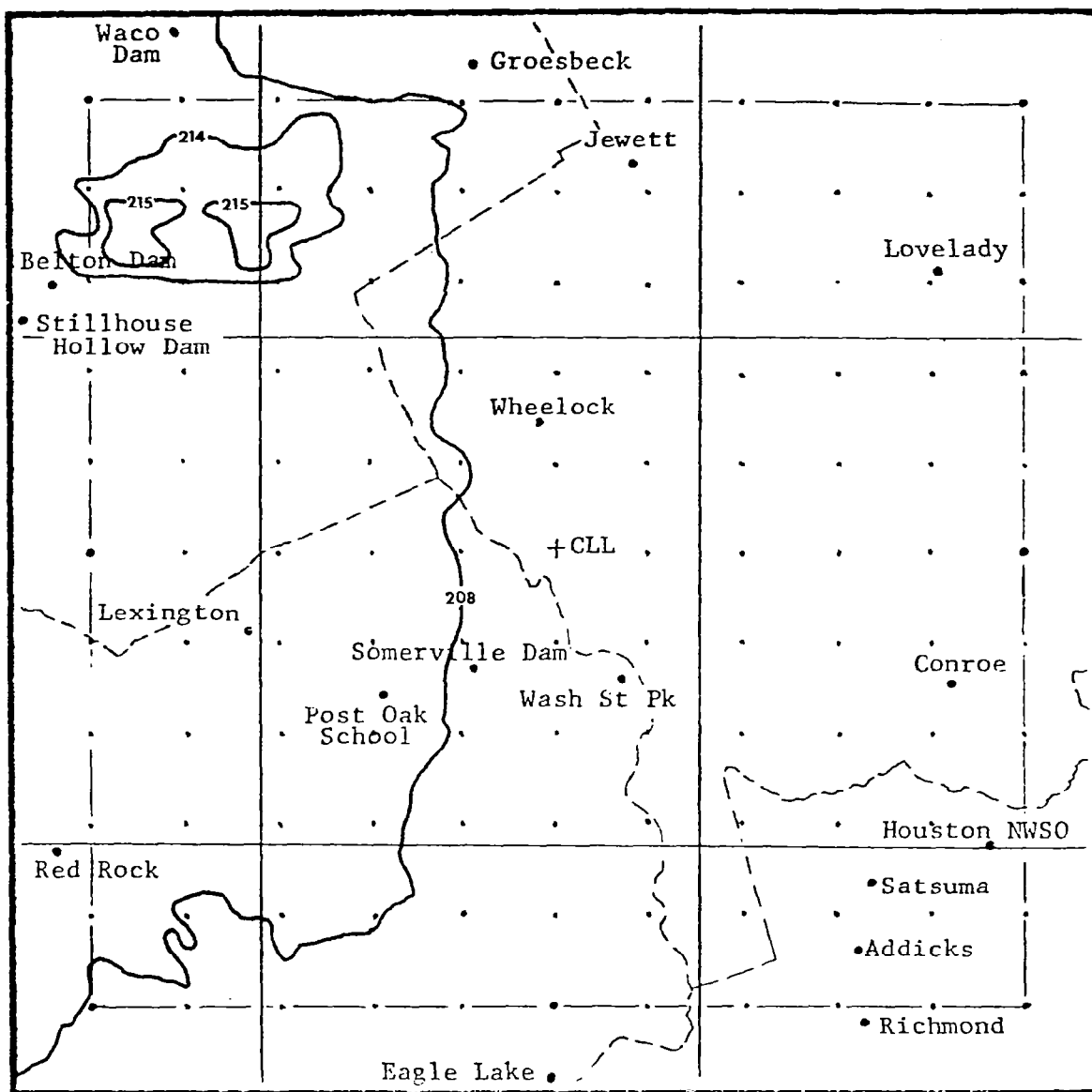


Fig. 16b. DCVM at 03/0115 GMT.

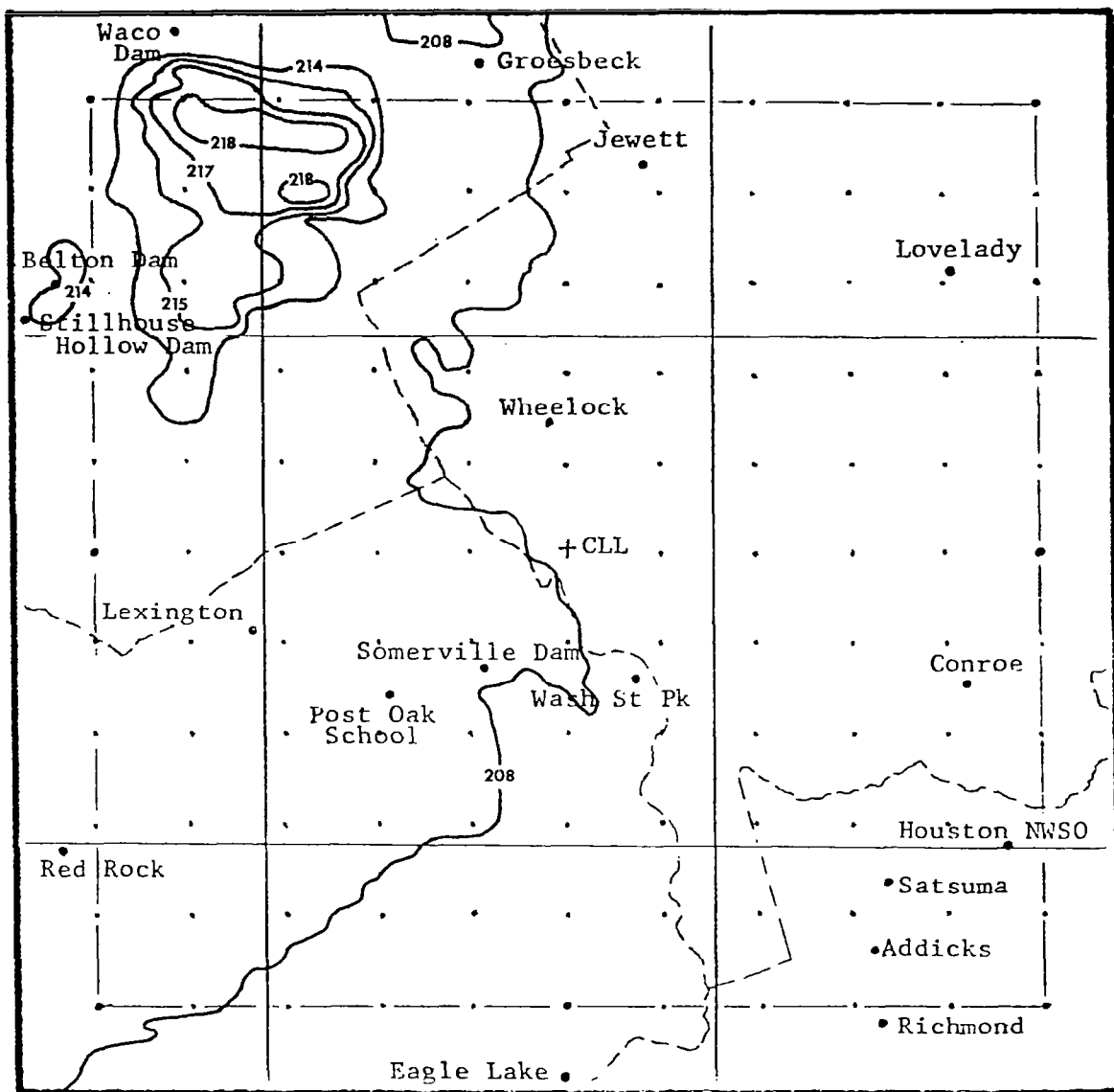


Fig. 16c. DCVM at 03/0130 GMT.

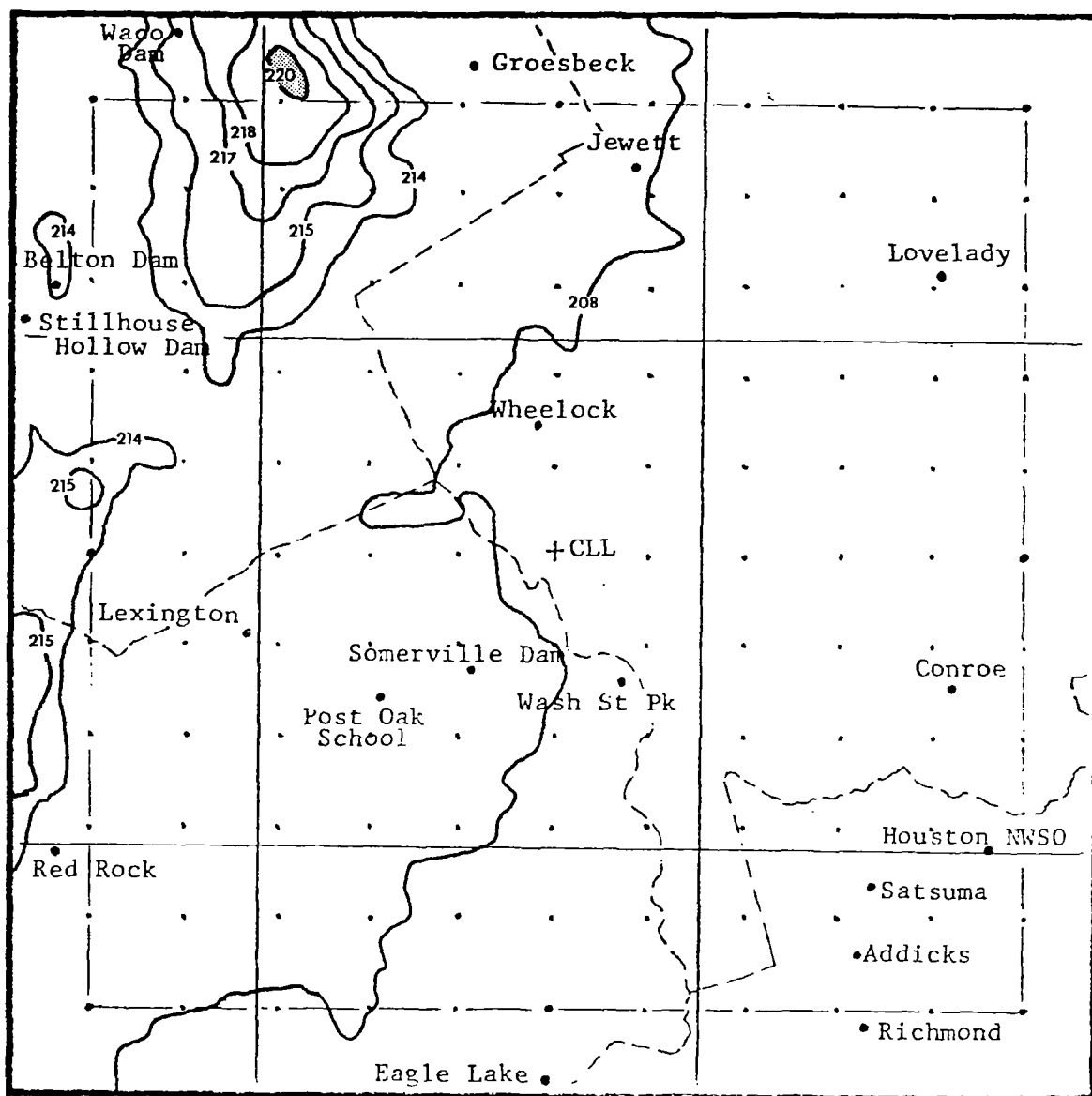


Fig. 16d. DCVM at 03/0145 GMT.

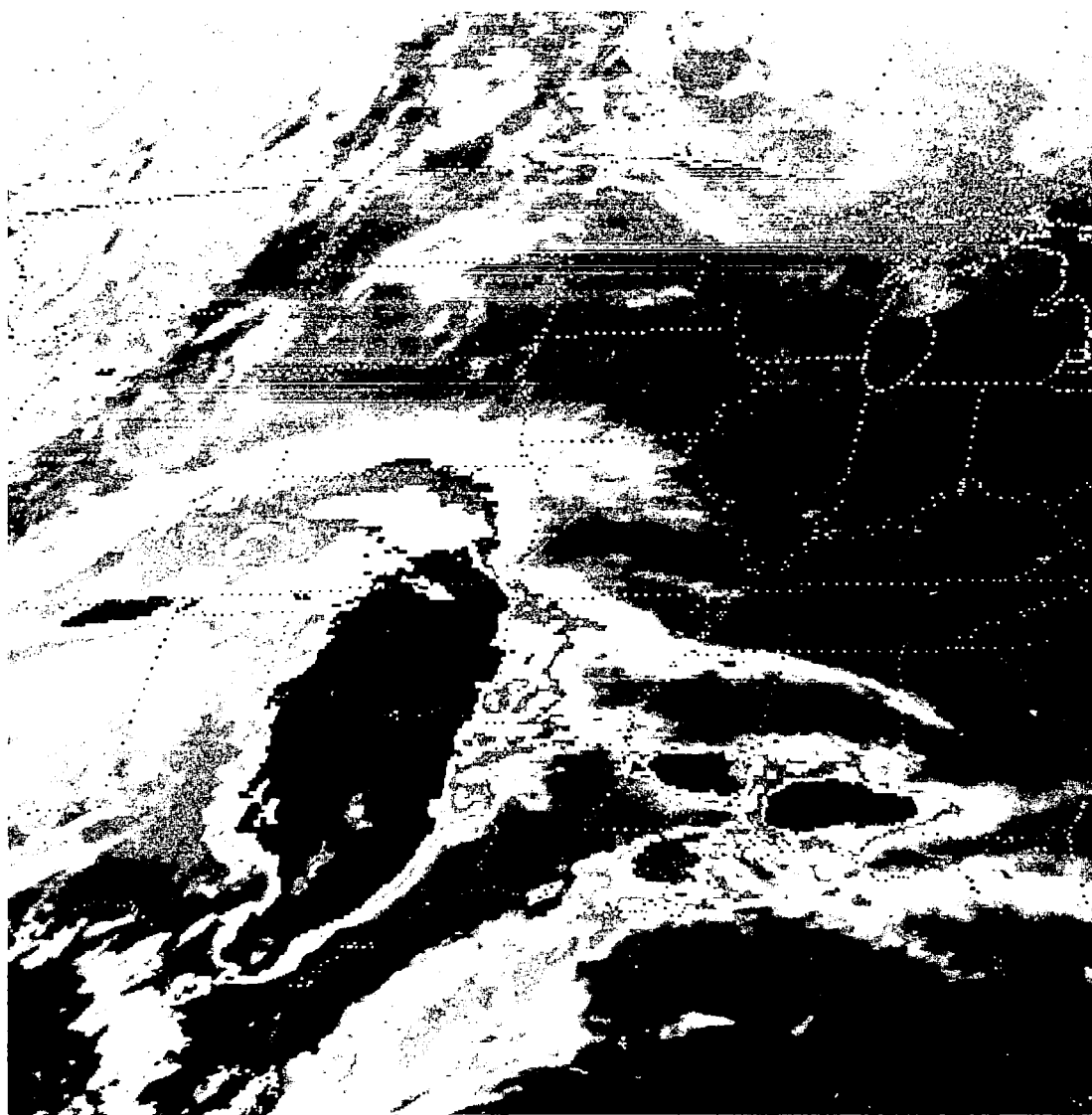


Fig. 17. 0200 GMT GOES-1 M_B EIR image.

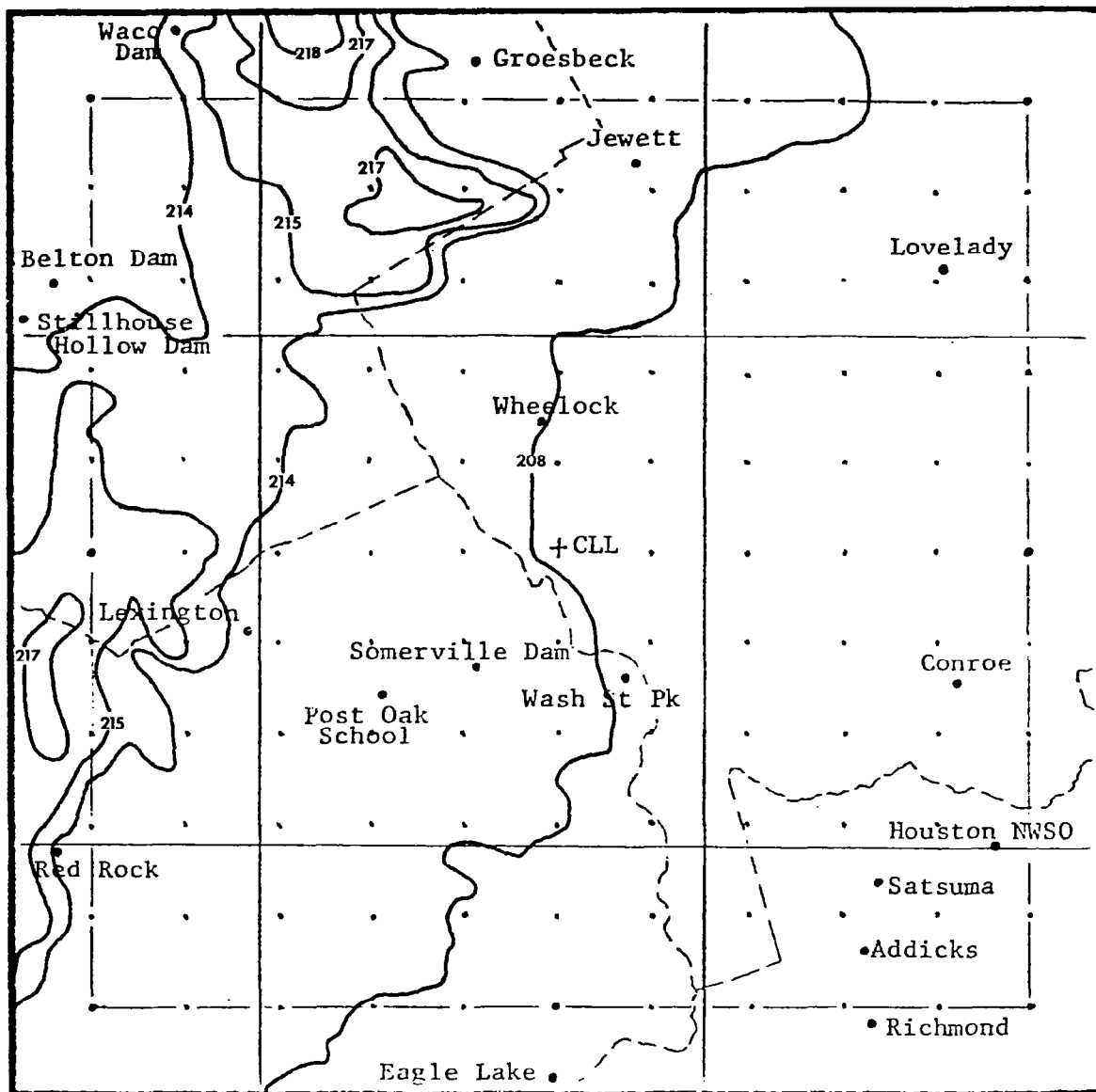


Fig. 18a. DCVM at 03/0200 GMT.

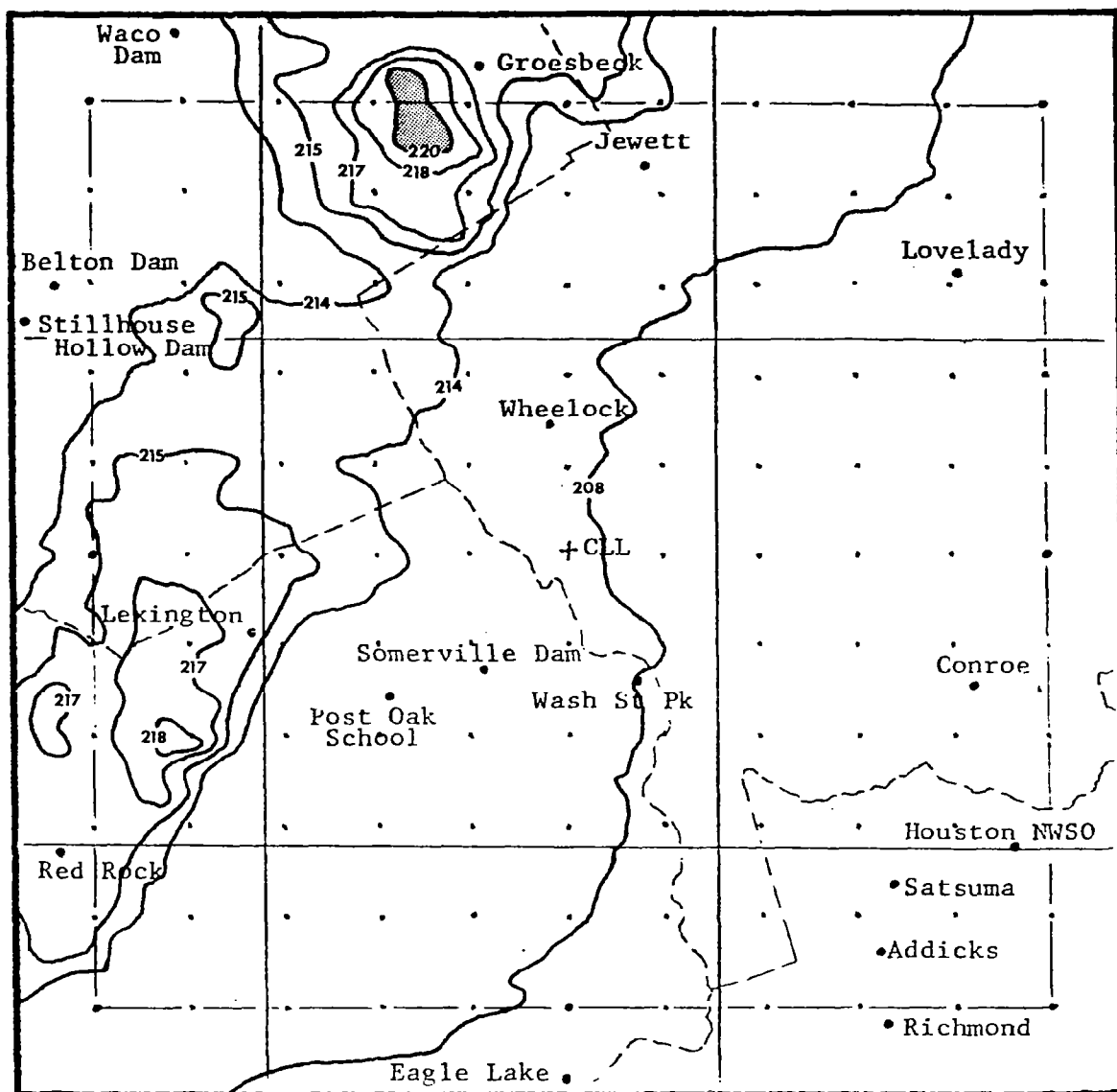


Fig. 18b. DCVM at 03/0215 GMT.



Fig. 19. 0230 GMT GOES-1 M_B EIR image.

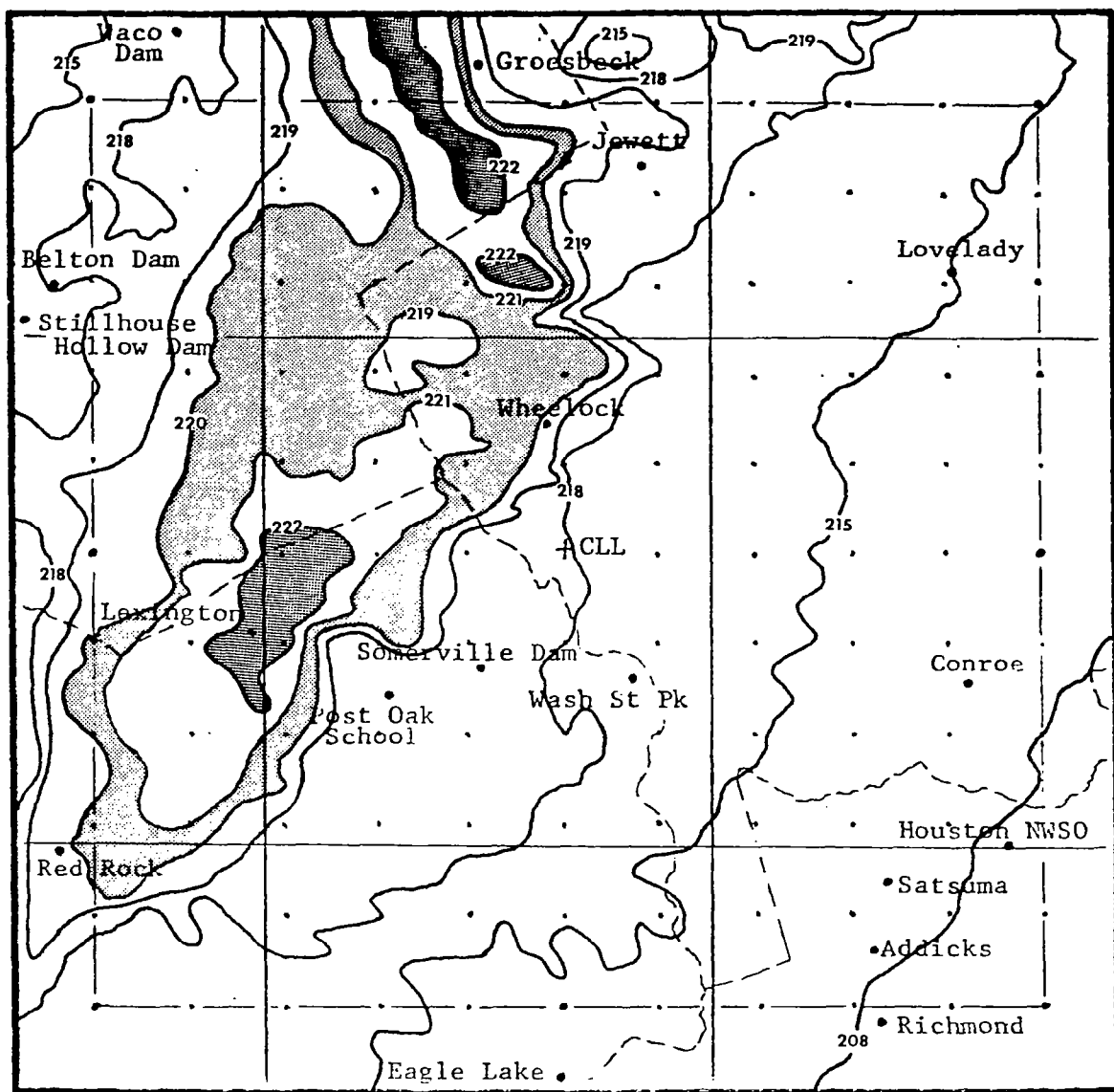


Fig. 20a. DCVM at 03/0230 GMT.

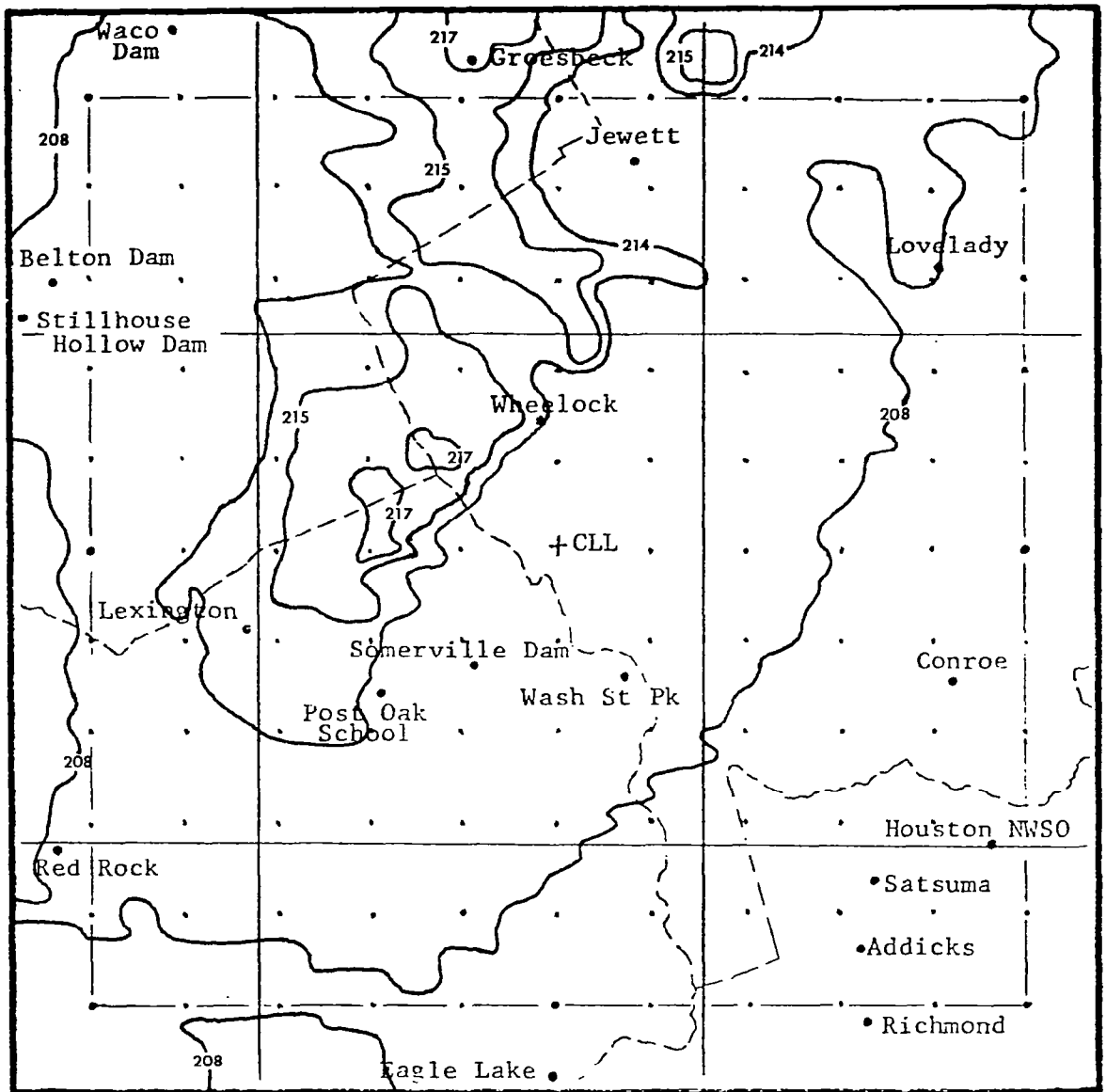


Fig. 20b. DCVM at 03/0245 GMT.

0215 GMT DCVMs depict the advance of the line of thunderstorms and their gradual strengthening prior to 0230 GMT. The 0230 GMT GOES image (Fig. 19) and DCVM (Fig. 20a) represent the period of maximum horizontal and vertical growth during the 3-h time frame. The second hour was the period of maximum rainfall also.

Fig. 19 best illustrates the concept introduced earlier, that only the very coldest tops are easily observed on the imagery. Note the area of bright white pixels in and on either side of the maximum activity in the thunderstorm line. A quick examination of Fig. 20a shows the region of high digital count values that are otherwise camouflaged in segment 8 (count 208-225) of the M_B enhancement curve. The 0245 GMT DCVM (Fig. 20b) marks the collapse of the strongest period that was occurring in the previous DCVM and denotes the initial stages of decay of the system as a whole. Fig. 20b corresponds to the end of the hour of heaviest precipitation (compare with Fig. 11, p. 32).

The 0300 GMT satellite image (Fig. 21) substantiates the thesis of storm decay by exhibiting a warming in the vicinity of the overshooting tops thresholds. Additional breakdown of the system in general is depicted by the remaining DCVMs (Figs. 22a-d). The final GOES-1 M_B EIR image at 0400 GMT (Fig. 23, which should be compared with Fig. 19) displays the weakened, steady state of the activity in East Texas.

At this point, it may prove meaningful to suggest that the DCVMs are also valuable when locating a collapse of an overshooting tops condition. As noted above, not only does the DCVM quickly establish

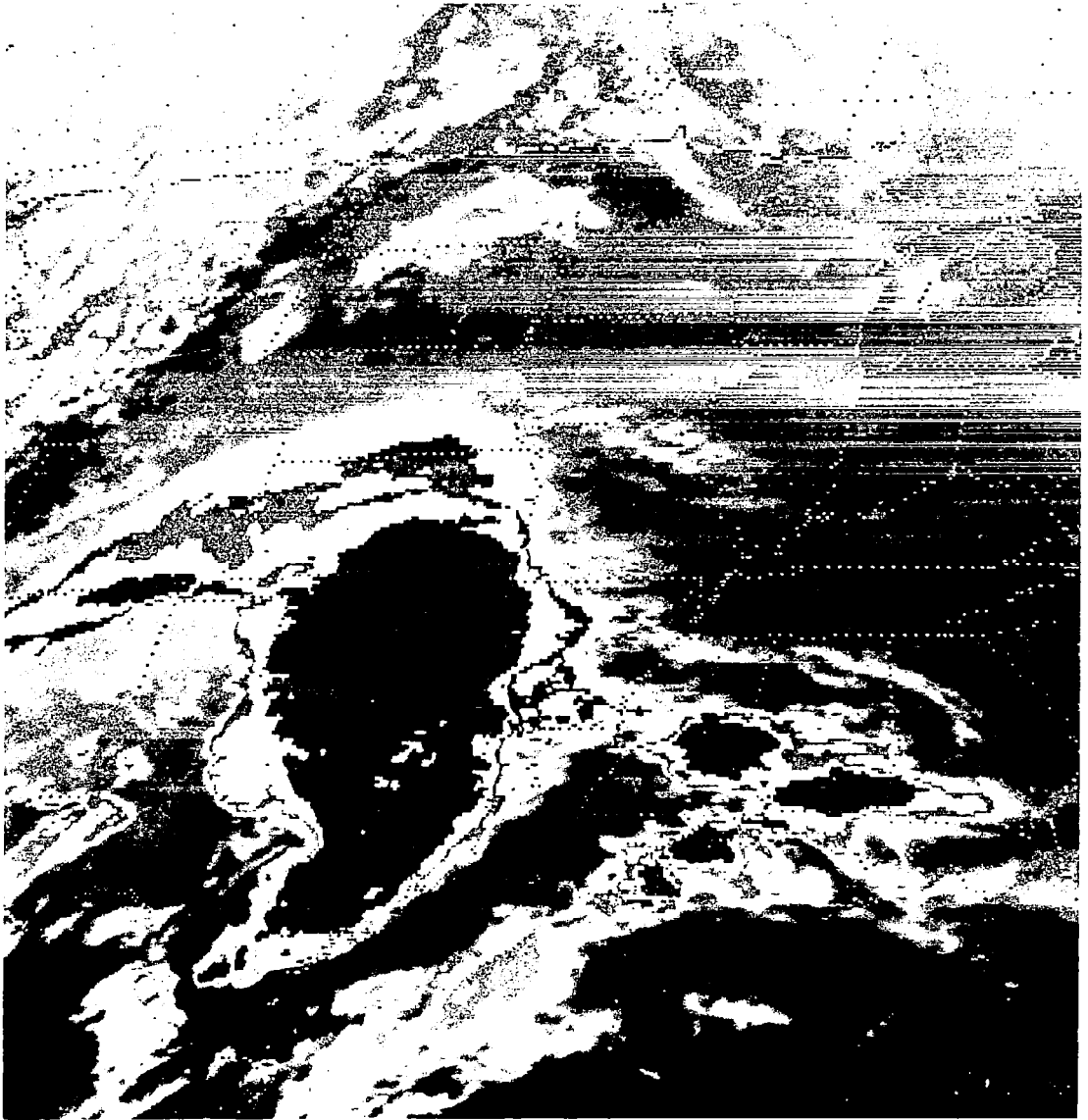


Fig. 21. 0300 GMT GOES-1 M_B EIR image.

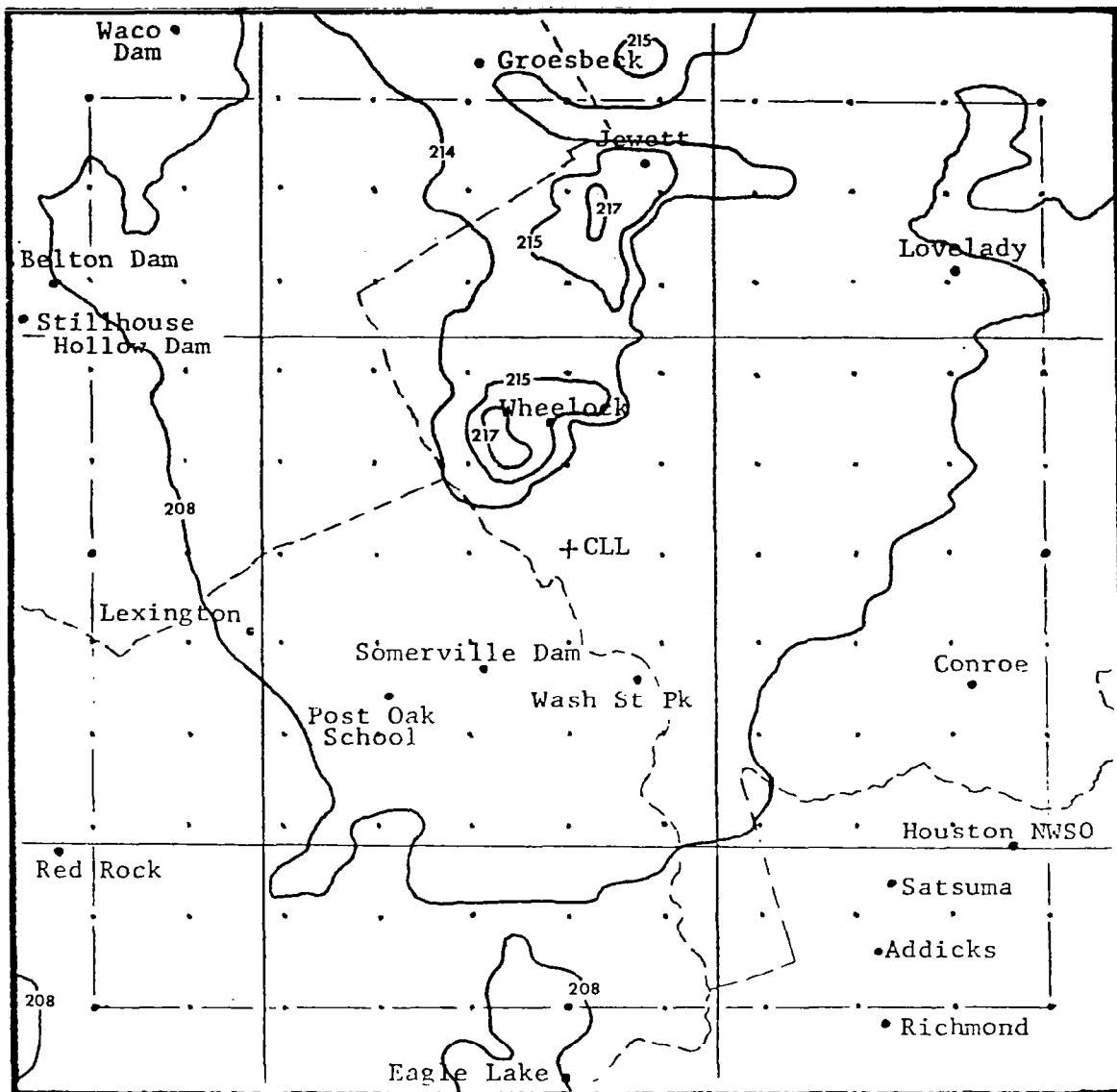


Fig. 22a. DCVM at 03/0300 GMT.

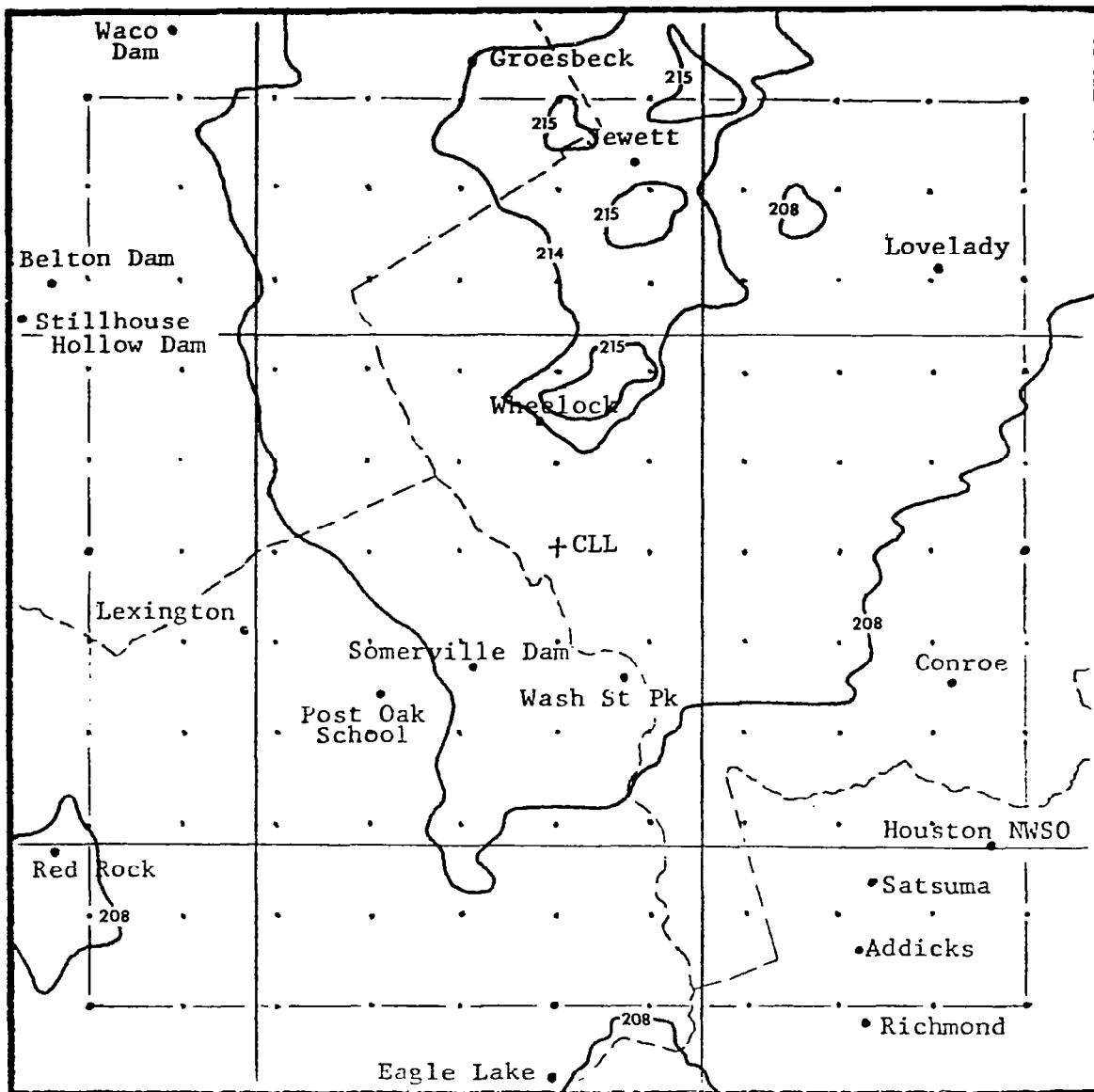


Fig. 22b. DCVM at 03/0315 GMT.

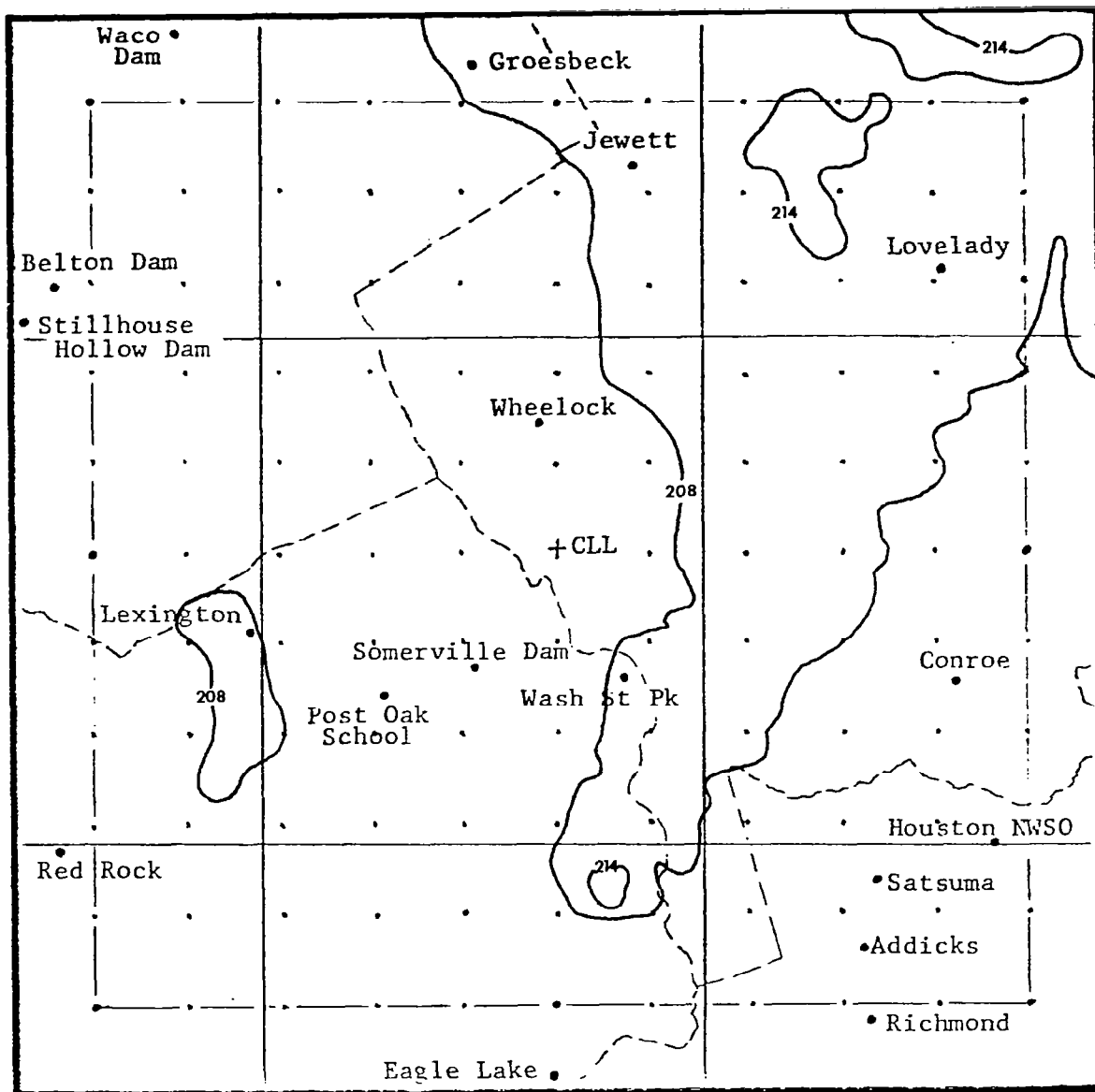


Fig. 22d. DCVM at 03/0345 GMT.

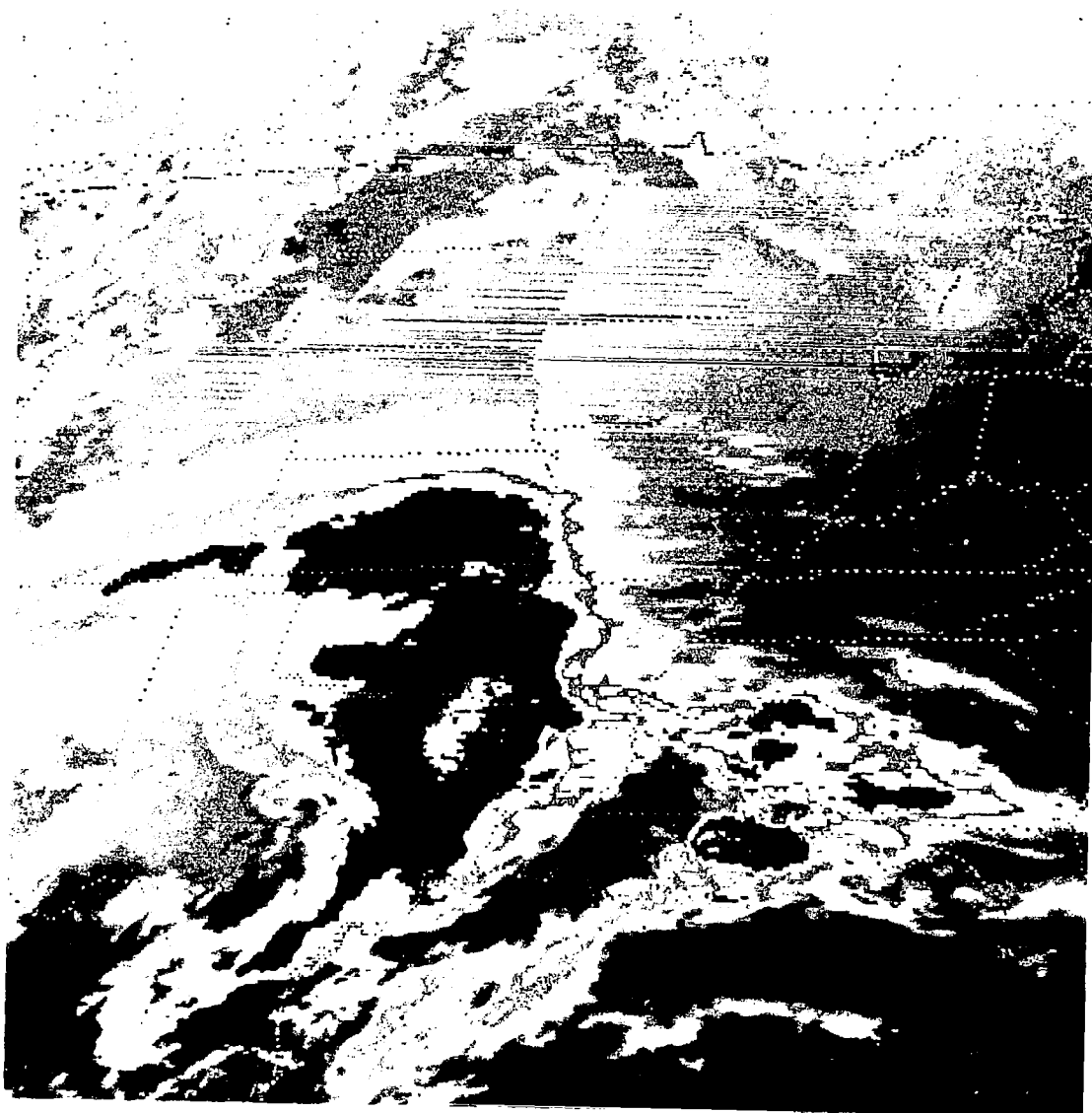


Fig. 23. 0400 GMT GOES-1 M_B EIR image.

the coldest region of the cloud, but it also clarifies any question that an observer might have when trying to determine whether he is looking at a light shade of gray (as in segment 5) corresponding to a much warmer temperature, or a colder portion (segment 8) of the M_B EIR curve. To illustrate this argument, compare Figs. 19, 21, and 23. Without similar time frame DCVMs (Figs. 20a, 22a, and 22d) one could easily misinterpret the shades of gray and the conditions that are occurring in the atmosphere. The DCVMs prove that the count values corresponding to Fig. 23 are not as high (cold) as those of either Fig. 19 or Fig. 21.

d. The Satellite-Derived Rainfall Estimations

As mentioned earlier, the digital count value 208 was selected by empirical methods as the boundary threshold to indicate convective precipitation. The count values less than 208 were, therefore, considered as areas having little or no precipitation and were not used in this objective study. Since the Scofield and Oliver (1977) M_B EIR imagery technique uses temperature threshold values rather than digital count values as in this investigation, the application of their rainfall scheme required some adjustment. Naturally, this adjustment assumes that the overshooting tops criterion is expected or has already occurred. The basic change that was made was to expand Scofield and Oliver's "step 4" (estimates applying to the two coldest contours) of their rainfall estimation scheme.

Since the rainfall estimation scheme using GOES imagery uses the two coldest contours in a particular thunderstorm system, the major

difficulty that a user must overcome is the identification of these coldest contours. The contours displayed may depend also on the character of the enhancement curve. This is where the digital counts are most readily usable because the highest (coldest) values are identified almost effortlessly, thereby enabling the user to pinpoint more quickly the area of maximum rainfall.

Fig. 24 lists the rainfall amounts in $\text{mm } \frac{1}{2}\text{h}^{-1}$ that were applied in using the cloud growth category versus digital count values in this study. Each count value in the left-hand column relates to a specific cloud top equivalent blackbody temperature. The next three columns relate the growth of the major axis of digital count contours between specific intervals of the DCVMs. These correspond to anvil growth rates that Scofield and Oliver used in their rainfall estimation scheme for $\frac{1}{2}\text{-h}$ intervals. The rainfall amounts in $\text{mm } \frac{1}{2}\text{h}^{-1}$ also were adapted from their imagery technique. The $\frac{1}{2}\text{-h}$ amounts were converted to $\text{mm } \frac{1}{2}\text{h}^{-1}$ for digital count values corresponding to their temperature thresholds. Appendix A outlines how the original breakdown of digital count values versus $\text{mm } \frac{1}{2}\text{h}^{-1}$, as displayed in Fig. 24, was devised.

The satellite-derived rainfall estimates were arrived at by using an objective approach. The first decision made was to select the manner by which each hour's DCVMs would be handled. Again, by empirical methods, it was determined that the first four DCVMs of the individual hour would give an adequate representation of the hour's rainfall. This approach was used to keep the method as simple and straightforward as possible and also to prevent data overlap, which could possibly introduce some additional small errors.

Digital Count Value	<u>Increase in major axis of Anvil</u> (along major axis of contour)			Digital Count Value Same or Decreased to not less than the 208 count value	Decayed to less than 208 count value
	> 75 km	38-75 km	≤ 37 km		
208	11.5	7.5	3.0	2.0	Trace
209	11.5	7.5	3.0	2.0	
210	11.5	7.5	3.0	2.0	
211	11.5	7.5	3.0	2.0	
212	11.5	7.5	3.0	2.0	
213	11.5	7.5	3.0	2.0	
214	13.5	8.5	4.0	3.0	
215	14.0	8.5	4.0	3.0	
216	14.5	8.5	5.0	3.0	
217	15.0	8.5	5.0	4.0	
218	15.5	8.5	5.0	4.0	
219	16.0	9.0	6.0	4.0	
220	16.5	9.0	6.0	4.5	
221	17.0	9.0	6.0	4.5	
222	17.5	9.0	6.0	4.5	
223	18.0	9.0	6.0	5.0	
224	18.5	9.0	6.0	5.0	
225	19.0	9.0	6.0	5.0	

Fig. 24. Rainfall in $\text{mm } \frac{1}{2}\text{h}^{-1}$ based on the growth or decay of the area of digital count value (adapted from Scofield and Oliver, 1977).

Basically, the rainfall estimation scheme as developed from Fig. 24 for the first hour is as follows:

(1) The 0100 GMT DCVM.

- (a) $3 \text{ mm } \frac{1}{4}\text{h}^{-1}$ inside 208 contours (growth less than 37 km).
- (b) $4 \text{ mm } \frac{1}{4}\text{h}^{-1}$ inside 214 contours (growth less than 37 km).

(2) The 0115 GMT DCVM.

- (a) $2 \text{ mm } \frac{1}{4}\text{h}^{-1}$ inside 208 contours (no change).
- (b) $8.5 \text{ mm } \frac{1}{4}\text{h}^{-1}$ inside 214-215 contours (growth 38-75 km).

(3) The 0130 GMT DCVM.

- (a) $2 \text{ mm } \frac{1}{4}\text{h}^{-1}$ inside 208 contours.
- (b) $3 \text{ mm } \frac{1}{4}\text{h}^{-1}$ inside 214-215 contours (no change).
- (c) $5 \text{ mm } \frac{1}{4}\text{h}^{-1}$ inside 217-218 contours (growth under 37 km).

(4) The 0145 GMT DCVM.

- (a) $2 \text{ mm } \frac{1}{4}\text{h}^{-1}$ inside 208 contours.
- (b) $3 \text{ mm } \frac{1}{4}\text{h}^{-1}$ inside 214-215 contours (no change).
- (c) $4 \text{ mm } \frac{1}{4}\text{h}^{-1}$ inside 217-218 contours (no change).
- (d) $6 \text{ mm } \frac{1}{4}\text{h}^{-1}$ inside 220 contours (growth less than 37 km).

This yields a total estimate for the hour of 0100-0200 GMT in mm.

After the amount of precipitation was determined for each DCVM, the next step was to add them graphically. Before each analysis was concluded, it was necessary to displace the estimates an average of 12 km toward the satellite subpoint to correct for the apparent location of the cloud versus the actual position of the cloud due to earth curvature. This procedure is recommended by Weiss (1978) and is outlined in Appendix B. Fig. 25 represents the graphic addition of DCVMs for 0100, 0115, 0130, and 0145 GMT by use of the estimation scheme outlined above. The same methods were used to determine Fig. 26 and Fig. 27, the second and third hour, respectively.

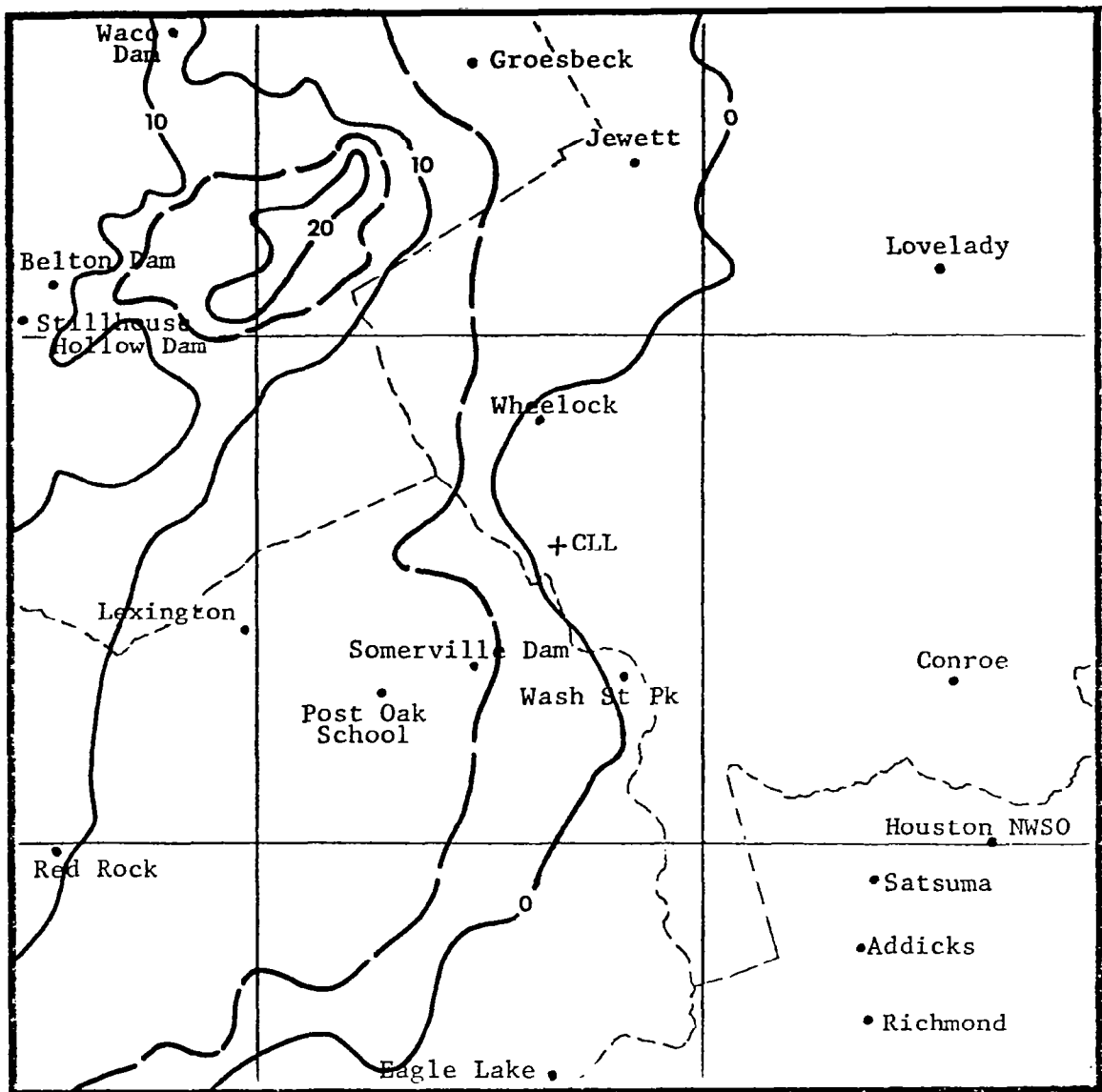


Fig. 25. The satellite-derived rainfall estimation analysis for the first hour (0100-0200 GMT).

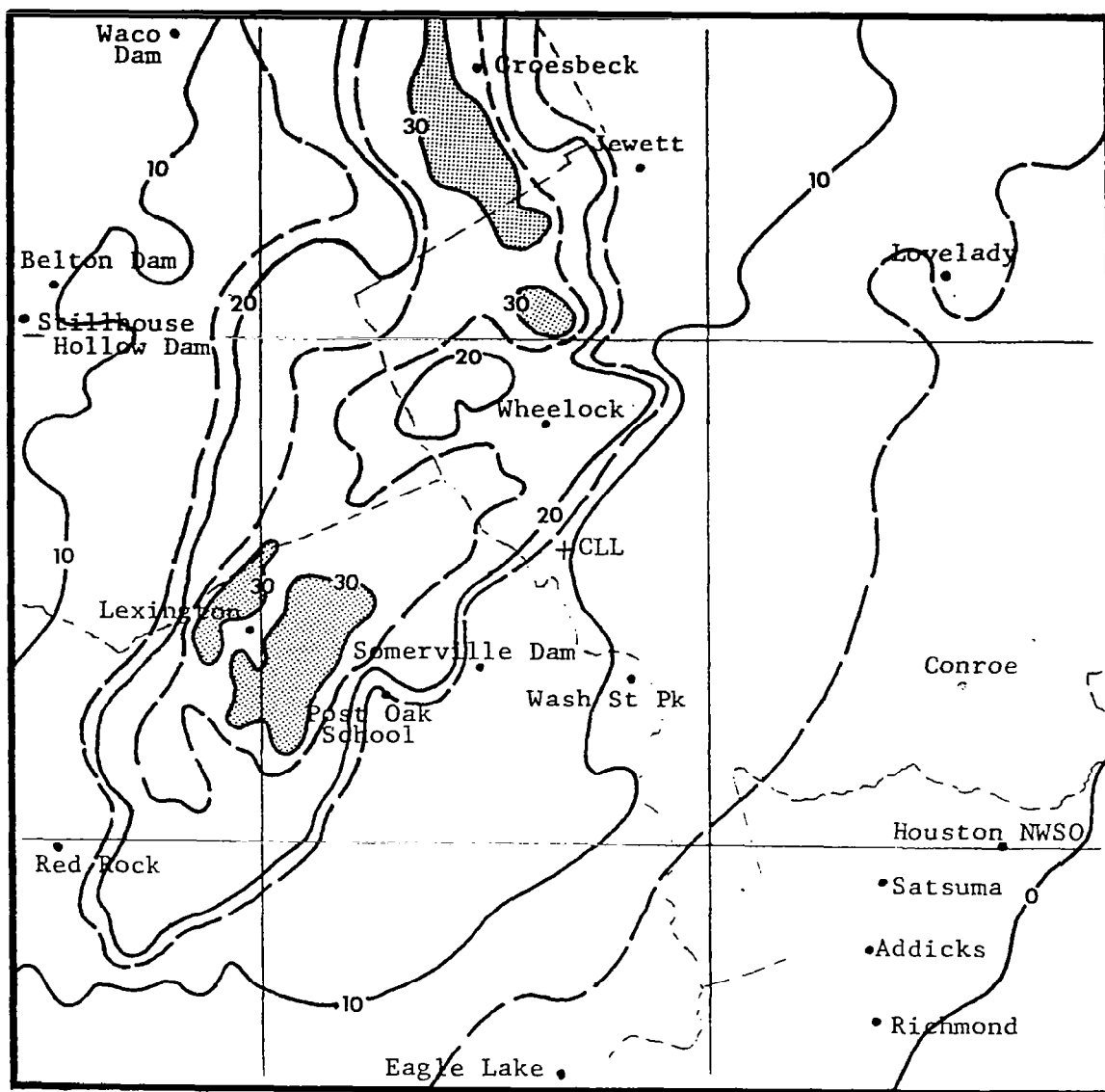


Fig. 26. The satellite-derived rainfall estimation analysis for the second hour (0200-0300 GMT).

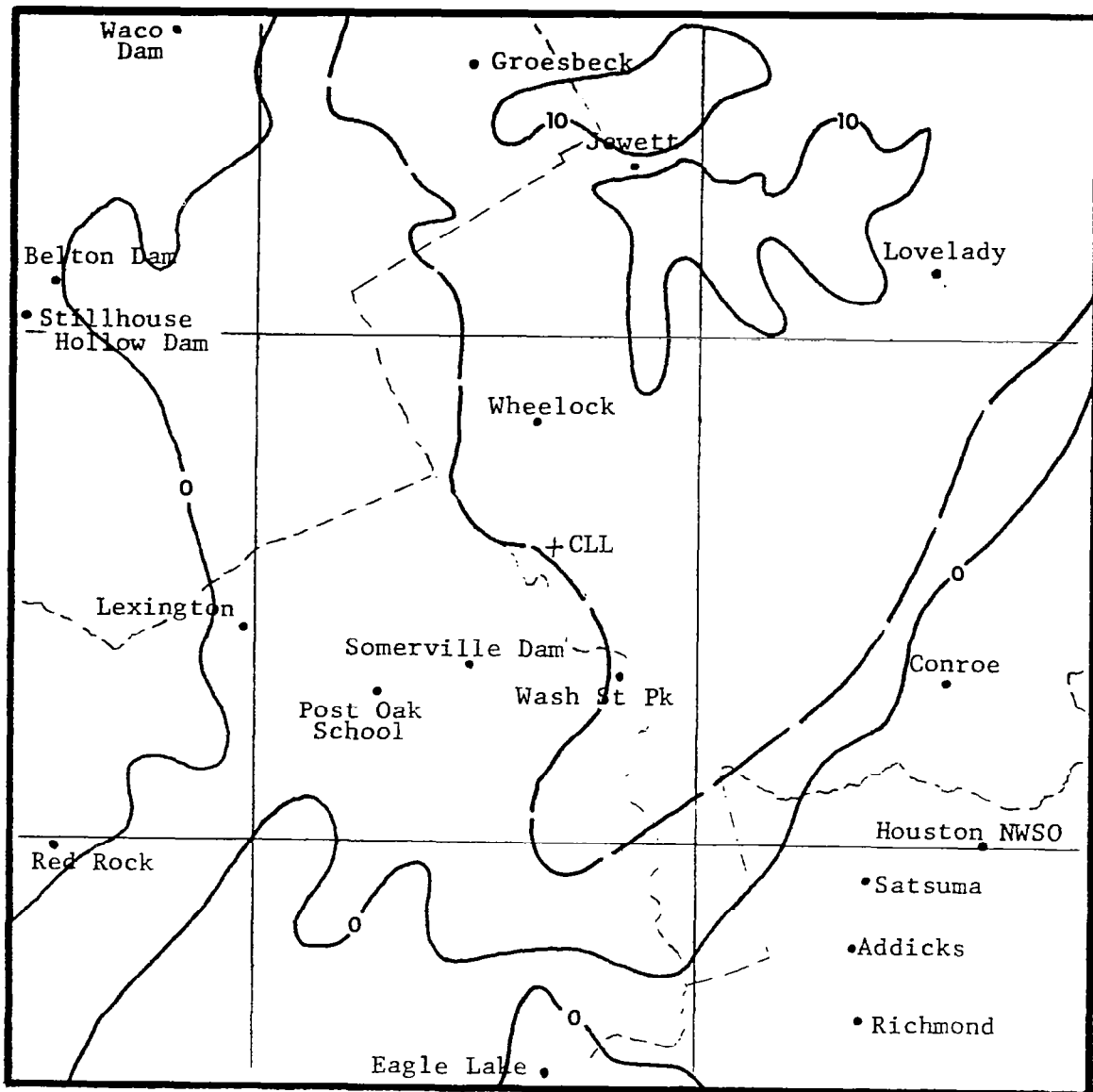


Fig. 27. The satellite-derived rainfall estimation analysis for the third hour (0300-0400 GMT).

The first and third hour rainfall estimations were quite simple and straightforward. The second hour estimation analysis, however, was somewhat complicated. The 0230 GMT DCVM depicts the case of extreme overshooting tops. This is a situation where an amplification factor of $6.5 \text{ mm } \frac{1}{2}\text{h}^{-1}$ (as Scofield and Oliver endorse) must be incorporated into the analysis to account for the increased rainfall that is usually observed under such conditions. This situation is handled so that the top digital count value contour (in this case, 222) is determined as the area that receives the $6.5 \text{ mm } \frac{1}{2}\text{h}^{-1}$ of additional rainfall. This criterion was adapted to account for an anvil increase greater than 37 km when the digital count values also increase 5 or more counts (e.g., from 217 to 222) over a 30-min interval at levels at and above the tropopause. The 0230 GMT DCVM was the explosive period that fulfilled this criterion since the tropopause was approximately at the 212 digital count level and the overshooting tops pushed 10 counts higher (10°C colder) as they increased 5 counts during the 30-min interval prior to 0230 GMT. If the highest count level fulfilled all requirements except the 37-km anvil increase, the next lower count contour would be used if it was still above the 5 count increase.

The final step in this phase was to add graphically the individual hourly analyses into a 3-h total and produce a satellite-derived rainfall estimation analysis for this portion of the storm (Fig. 28). Table 4 depicts the amounts of rainfall derived at actual stations via this rainfall scheme for each hourly interval and the 3-h total.

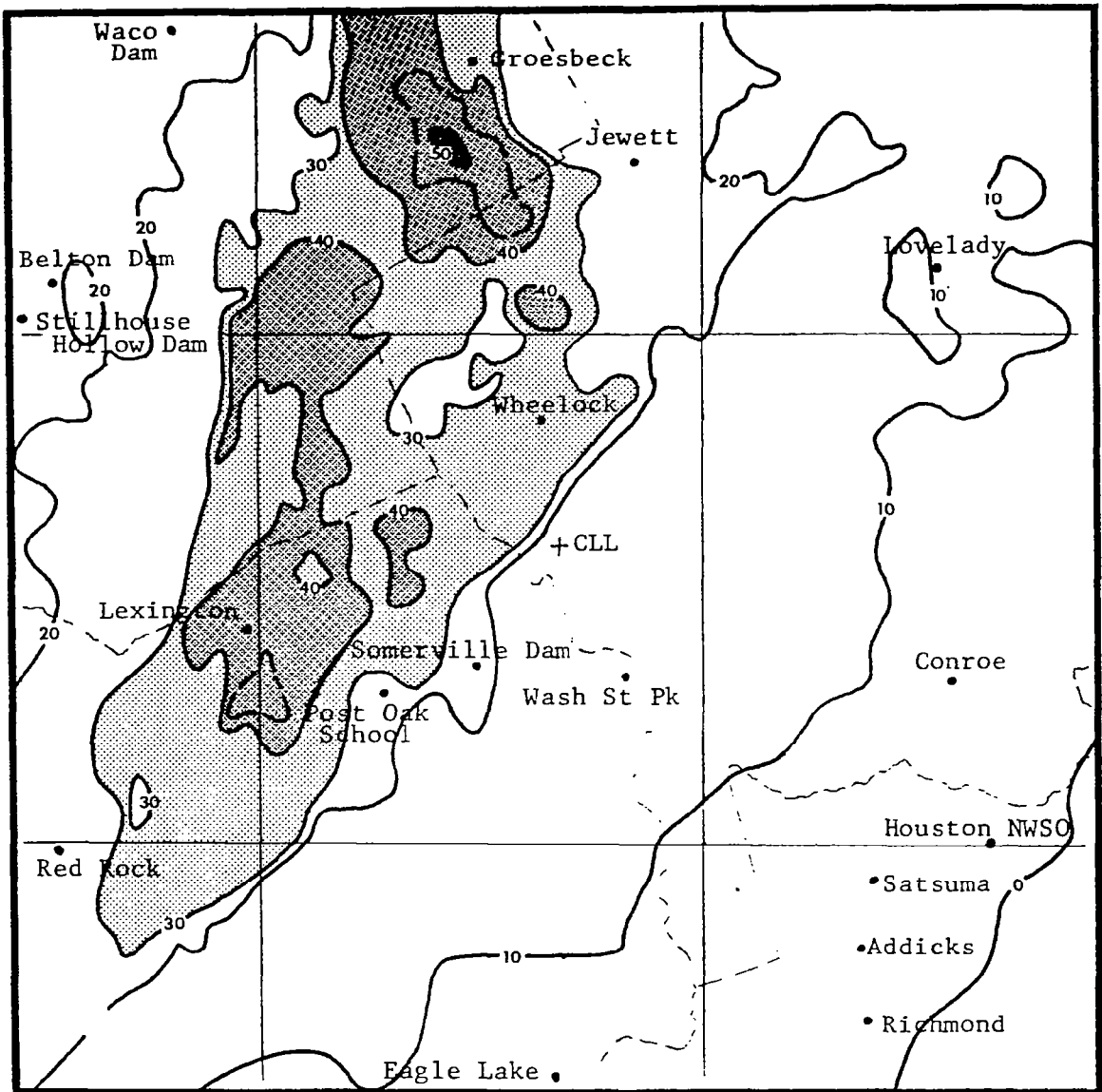


Fig. 28. The 3-h total of satellite-derived rainfall estimation analyses (0100-0400 GMT).

Table 4. Hourly rainfall estimates and 3-h total in mm.

Location	First hour	Second hour	Third hour	3-h total
Belton Dam	9	9	0	18
Conroe	0	2	0	2
Eagle Lake	0	2	2	4
Groesbeck	2	27	10	39
Houston-WSMO	0	2	0	2
Houston-Addicks	0	2	0	2
Houston-Satsuma	0	2	0	2
Jewett	2	10	11	23
Lexington	9	29	2	40
Lovelady	0	6	8	14
Post Oak School	6	11	3	20
Red Rock	10	11	0	21
Richmond	0	2	0	2
Somerville Dam	6	10	4	20
Stillhouse Hollow Dam	9	9	0	18
Waco Dam	9	9	0	18
Washington State Park	0	8	4	12
Wheelock	0	24	7	31

e. Comparisons

To compare properly the observed rainfall patterns to the satellite-derived rainfall patterns, it is important to relate the subjectivity of the raingage analyses. The raingage analyses were accomplished in a subjective manner inasmuch as the major part of the study area was without a well-defined, high-resolution, raingage network. The basic field, as outlined earlier, was analyzed from 18 separate hourly recording stations. Even though these analyses were approached as objectively as possible, they will always be somewhat biased towards the individual performing the analysis. Furthermore, the 3-h total analysis (Fig. 13, p. 34) was performed similiarly to the hourly analyses with two additional restraints. The first restraint was that the 3-h analysis pattern had to fit graphically the addition of the individual analyses when they were combined, and the second, that the 3-h total rainfall pattern could not exceed the 24-h analysis pattern (also derived subjectively, but with a greater number of reporting stations). On the other hand, the satellite-derived estimations are as objective as possible, within a range of certain reasonable restraints (Fig. 24, p. 58) to insure a field representative of the observed.

With these facts in mind, comparisons can now be made of the hourly rainfall segments and the 3-h total portion of the storm. To maintain unbiased data, the correlations are based on the hourly rainfall station data versus the satellite-derived estimations at each recording station rather than a comparison of the subjective hand

analyses. The individual hourly raingage analyses and their respective satellite-derived rainfall estimates will be discussed first, followed by the comparisons between the 3-h total observed versus estimated data.

The first hour's data (Fig. 10, p. 31 and Fig. 25, p. 60) show similiarity with respect to the orientation of the rainfall pattern. Of particular interest are the first and third hour's rainfree areas and how they nearly match the observed when compared to the estimated. The observed versus estimated correlation for the first hour was 0.57 for the 18 data pairs of information taken from Tables 2 and 4 (p. 29 and p. 65). This was as expected because the rainfall amounts were low, which tended to allow the rainfall pattern to be more variable.

The second hour received the most precipitation and the satellite estimates substantiate this (Fig. 11, p. 32 and Fig. 26, p. 61). Since the main thrust of this investigation is toward flash flood-type situations, it was important to discover the location of heavy precipitation areas. The satellite estimation method exhibits ability for accomplishing this task. Two distinct regions of precipitation totaling 30 mm or greater are seen in both the observed and estimated analyses. Both analyses are in good agreement with their general rainfall patterns, and their 18-station data pair correlation was 0.85. This supports the statement that was alluded to in the above paragraph, that heavier rainfall will be more reliably indicated in the estimation technique, which will potentially provide more usable information to operational forecasters.

The third hour (Fig. 12, p. 33 and Fig. 27, p. 62) was much like

the first, with less precipitation and a fairly widespread rainfall pattern. The northeast quadrant of the estimate depicts rainfall similiar to that observed. In the Post Oak School and Somerville Dam areas, however, it misses by over 10 mm. The third hour correlation was 0.56, about as expected.

The 3-h total rainfall data sets will now be discussed. These data estimates should be considered separately from the hourly comparisons and correlations because they were developed from those sets and remain dependent upon them. If the 3-h interval (0100-0400 GMT) was considered as the amount of time the "storm" took to cross the study area, then all the rainfall that was estimated would represent the storm's total. It is in this perspective that the 3-h total should be regarded. The data that covered the life of the storm would have the best rainfall patterns and correlations since the estimation technique is primarily based on four of the five DCVMs available for each hour. The small data loss, which was anticipated during each hour, will be recovered when the period of the storm is considered and the rainfall estimates for each hour are added up.

Consequently, a comparison of the 3-h observed and estimated analyses (Fig. 13, p. 34 and Fig. 28, p. 64) indicates that the rainfall patterns are strikingly similiar in areal extent for amounts up to 30 mm and somewhat more widespread for greater amounts. Even though it seems obvious, it is worthwhile to note that isolated point values, represented by the raingages, would not (in a general case such as this) be expected to report the maximum amount of rain from a convective system. With this in mind we can continue our comparisons. The

raingage analysis places the 40-mm isohyets over a smaller areal expanse than the satellite estimates. Rainfall appears to be over-estimated between Groesbeck and Lexington. This is confirmed if Fig. 9 (p. 28), the 24-h rainfall, is used as the upper limit of the precipitation. A visual comparison of the raingage analyses for 24-h and 3-h, and the 3-h satellite-derived estimate shows that the 3-h raingage analysis could be expanded, and then the comparisons between the observed and estimated would improve somewhat. The 18-station data pair correlation was 0.90. An examination in and around the Houston area, located in the southeast quadrant, indicated that little or no convective-type precipitation fell before 0400 GMT. Therefore, if the four reporting stations (Houston WSMO, Addicks, Satsuma, and Richmond) located in the southeast portion of that quadrant were removed from the station data pairs the correlation would improve to 0.92.

Even though the 3-h 40-mm estimated contours appear larger than the 3-h observed 40-mm contours, they do provide valuable information and help to pinpoint heavy rainfall areas with reasonable accuracy. Table 5 was developed from Tables 2 and 4 and is offered as a quick comparison between the observed (raingage) and estimated (satellite) rainfall and the correlations computed each time interval.

As mentioned earlier in the supplemental data section, the TAMU radar total VIL maps for selected areas were compared visually to DCVMs having a similiar time frame. Fig. 29 shows the 0223 GMT total VIL map superimposed on the displaced 0230 GMT satellite DCVM. Henderson (1979) examined this same time frame and computed a

Table 5. Hourly and 3-h observed and estimated rainfall in mm.

Location	First		Second		Third		3-h Total	
	Obs	Est	Obs	Est	Obs	Est	Obs	Est
Belton Dam	4	9	7	9	0	0	11	18
Conroe	0	0	0	2	0	0	0	2
Eagle Lake	0	0	0	2	5	2	5	4
Groesbeck	3	2	36	27	5	10	44	39
Houston-WSMO	0	0	3	2	0	0	3	2
Houston-Addicks	1	0	1	2	13	0	15	2
Houston-Satsuma	0	0	1	2	0	0	1	2
Jewett	0	2	8	10	16	11	24	23
Lexington	3	9	33	29	5	2	41	40
Lovelady	0	0	0	6	14	8	14	14
Post Oak School	2	6	1	11	17	3	20	20
Red Rock	0	10	20	11	0	0	20	21
Richmond	0	0	1	2	4	0	5	2
Somerville Dam	3	6	0	10	13	4	16	20
Stillhouse Hollow Dam	4	9	4	9	0	0	8	18
Waco Dam	12	9	4	9	1	0	17	18
Washington State Park	0	0	3	8	8	4	11	12
Wheelock	4	0	11	24	3	7	17	31
18-station correlation	0.57		0.85		0.56		0.90	

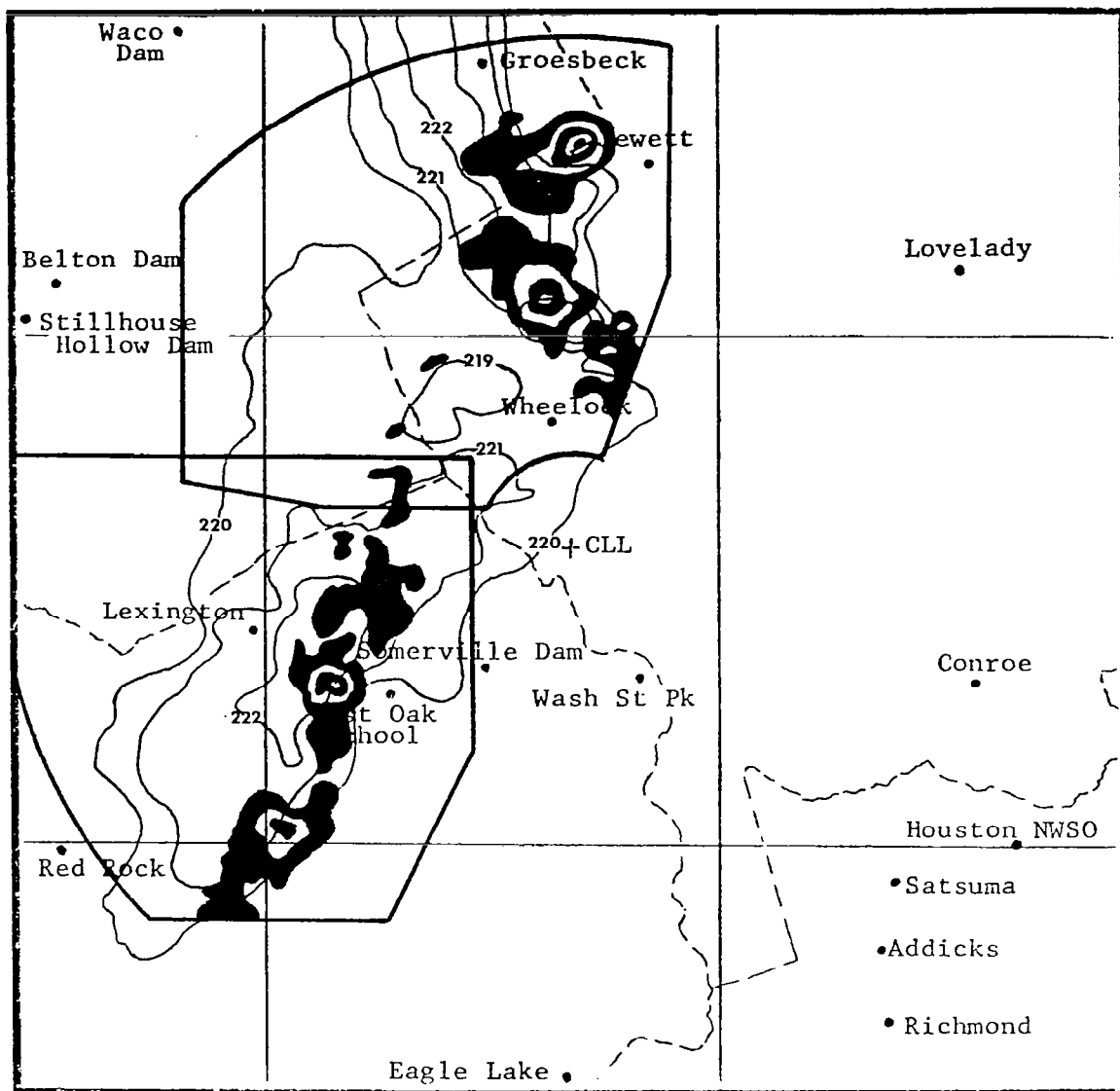


Fig. 29. The 0223 GMT total VIL map superimposed on the displaced 0230 GMT DCVM. The radar VIL isopleths begin with the analyzed values of 10 to 19 for the first blackened contour, and thereafter alternate with white, in steps of 10, until the highest VIL values of 50-plus were detected approximately 20 km west of Jewett.

correlation of 0.39 for the northwest quadrant and a correlation of 0.40 for the southwest quadrant. The figure clearly shows that the fields do not match up perfectly, but they do demonstrate some significant relationship. Additional total VIL maps were not available to pursue these comparisons further at this time. McAnelly (1979), however, is currently conducting research with these goals in mind.

6. CONCLUSIONS

This study demonstrated that an objective satellite-derived rainfall estimation technique is feasible with use of digital GOES IR data. Although these results are based only on one case, it appears that this approach can pinpoint areas of heavy, as well as lighter, precipitation with fairly accurate success. The ability to determine precipitation patterns and amounts in data-sparse areas would be an asset to many operational meteorologists, besides providing valuable information to support investigative, research programs regarding the water budget.

One of the shortcomings of the Scofield and Oliver (1977) rainfall estimation scheme is that it requires an experienced individual to interpret properly the GOES VIS and EIR imagery. This investigation requires that certain restraints be met and then uses the digital GOES IR data, which have the distinct advantage of 24-h surveillance of weather systems, to develop the precipitation estimates. The Scofield and Oliver (1977) and Scofield (1978a, 1978b) methodology requires careful interpretation of amplification factors. By contrast, I believe that the high digital count value variations in time and space will reveal objectively those situations where intense precipitation is occurring (e.g., merging cell and intersecting thunderstorm lines). Furthermore, since the overshooting tops condition is in and above the anvil top, it is conceivable that the upper-level wind effects for short time intervals, as in this study, can be somewhat neglected to obtain operational estimates of heavy rainfall.

One of the foremost obstacles that must be surmounted is the reduction of the vast quantities of data to suitable spatial resolution. This examination used McIDAS data, which have implied 4 km by 4 km resolution, to demonstrate relatively high resolution rainfall patterns with areal variations that closely resemble the observed analyses. This tends to strengthen the argument even more for this kind of approach.

The NWS currently is using the Scofield and Oliver method for estimating rainfall from hourly GOES M_B EIR imagery. Not only do they sacrifice resolution because of the mode of transmission of the imagery and the need to conserve manhours, they also may miss precipitation amplifiers that could very likely be sandwiched between the hourly intervals of the EIR data. The technique used in this study, on the other hand, approaches the state of the art without forfeiting additional manhours. At the same time it will vastly improve and resolve the widespread precipitation pattern that is presently based on hourly GOES M_B EIR imagery.

The DCVMs that were visually compared with the total VIL maps that were available indicated some fair correlations. One of the major problems could possibly be with the gridding, but I believe that a better understanding of cloud processes is necessary to reveal the true relationships between a VIL map and a DCVM.

Although this single case does not prove conclusively that the methodology used herein is without flaws, it does demonstrate reasonable accuracy with a correlation of 0.92 for the convective

study period of the storm. This type of correlation accounts for approximately 85% of the variability in the data. This leads to a final conclusion that an accurate objective rainfall estimation technique based on digital geostationary satellite data is feasible. Furthermore, it could be one that should be developed further for operational use by meteorologists and hydrologists responsible for flash flood prediction. It could spell the difference between adequate warning and disaster.

7. RECOMMENDATIONS

The following recommendations for use of digital GOES IR data for further satellite-derived rainfall estimation studies and flash flood detection investigation are presented:

- (1) This rainfall estimation approach should be tested against well-documented rainstorms (e.g., flash floods such as those at Big Thompson Canyon, Johnstown, and Kansas City) to enable formulation of more conclusive results. These studies should also attempt to account for the rainfall underestimations made by Scofield (1978b) for the point maximum of the raingage measurements.
- (2) Additional research efforts should incorporate digital VIS data which have 1 km by 1 km resolution. With the use of the McIDAS gridding program devised by Henderson (1979), even higher resolution rainfall patterns may be possible. Furthermore, the comparisons made from the two types of digital data (VIS and IR) could reveal interesting conclusions.
- (3) Due to the areal limitations placed on the McIDAS data used in this study (240 km by 240 km), Atmospheric and Oceanographic Information Processing System (AOIPS) data should be utilized to conduct similiar research. The main advantage of the AOIPS is that it covers vast expanses of the United States, thus allowing studies in different regions from the same data base.

- (4) Consideration should be given to expanding segment 8 (the repeat gray levels) of the M_B EIR curve and then enlarging suspect flash flood areas on the M_B enhanced GOES imagery. This could be applied to the Scofield and Oliver (1977) rainfall scheme for pinpointing heavy precipitation areas while digital rainfall estimation schemes are being developed.
- (5) An algorithm should be developed that will allow adjustment, if necessary, to different geographic regions that are under surveillance. Development of the scheme should be incorporated into a computer program as a first step toward operational use.
- (6) Warm and cold (low and high digital count variations) anvil areas should be investigated to enable comparisons that would lead to a better understanding of the variations of the rainfall patterns associated with them.
- (7) Total VIL maps and DCVMs should be rigorously compared to examine their relationship and to enable understanding of the cloud processes taking place.
- (8) A mini-computer program incorporating the topography of a hydrological region (e.g., water shed) should be utilized with the rainfall estimates derived from various means (subjectively and/or objectively) to aid the meteorologist and/or hydrologist in operational flash flood prediction.

REFERENCES

- Allison, L. J., E. B. Rogers, T. T. Wilheit, and R. W. Fett, 1974: Tropical cyclone rainfall as measured by the NIMBUS 5 electronically scanning microwave radiometer. Bull. Amer. Meteor. Soc., 55, 1074-1089.
- American Meteorological Society, 1978: Flash floods--a national problem. Bull. Amer. Meteor. Soc., 59, 585-586.
- Cherne, T. L., 1974: The scan plane method for locating and gridding scanning radiometer satellite data. Air Weather Service, AFGWC Tech. Memo. 74-1, Offutt Air Force Base, NB, 80 pp.
- Corbell, R. P., C. J. Callahan, and W. J. Kotsch, 1976: The GOES/SMS User's Guide. NOAA/NESS, Washington, D.C., 118 pp.
- Davis, J. G., H. E. Fuelberg, and R. E. Turner, 1978: NASA's AVE VII Experiment: 25-mb sounding data. NASA Tech. Memo. 78197, Marshall Space Flight Center, AL, 222 pp.
- Follansbee, W. A., 1973: Estimation of average daily rainfall from satellite cloud photographs. NOAA Tech. Memo. NESS 44, Washington, D.C., 33 pp.
- , and V. J. Oliver, 1975: A comparison of infrared imagery and video pictures in the estimation of daily rainfall from satellite data. NOAA Tech. Memo. NESS 62, Washington, D.C., 14 pp.
- Griffith, C. G., and W. L. Woodley, 1973: On the variation with height of the top brightness of precipitating convective clouds. J. Appl. Meteor., 12, 1086-1089.
- , ———, S. Browner, J. Teixeira, M. Maier, D. W. Martin, J. Stout, and D. N. Sikdar, 1976: Rainfall estimation from geosynchronous satellite imagery during the daylight hours. NOAA Tech. Rept. ERL 356-WPM07, Boulder, CO, 106 pp.
- , ———, and P. G. Grube, 1978: Rain estimation from geosynchronous satellite imagery--visible and infrared studies. Mon. Wea. Rev., 106, 1153-1171.
- Hawkins, R. S., 1977: A new automatic processing technique for satellite imagery analysis. Air Force Systems Command. AFGL-TR-77-0174, Hanscom Air Force Base, MA, 69 pp.
- Henderson, R. S., 1979: Digital meteorological radar data compared with digital infrared data from a geostationary meteorological satellite. M. S. Thesis, Texas A&M University, 103 pp.

- Lethbridge, M., 1967: Precipitation probability and satellite radiation data. Mon. Wea. Rev., 95, 487-490.
- Martin, D. W., and W. D. Scherer, 1973: Review of satellite rainfall estimation methods. Bull. Amer. Meteor. Soc., 54, 661-674.
- McAnelly, R. L., 1979: Private Communication.
- McKowan, P. L., 1977: VISSR data processing plan for synchronous meteorological and geostationary operational environmental satellites (SMS/GOES). Goddard Space Center Rept. X-565-77-219, Greenbelt, MD, 232 pp.
- Mogil, H. M., J. C. Monro, and S. G. Grant, 1978: NWS's flash flood warning and disaster preparedness programs. Bull. Amer. Meteor. Soc., 59, 690-699.
- Oliver, V. J., and R. A. Scofield, 1976: Estimation of rainfall from satellite imagery. Preprint Sixth Conf. on Weather Forecasting and Analysis, Albany, NY, Amer. Meteor. Soc., May, 1976, 242-245.
- Reynolds, D., and T. H. Vonder Haar, 1973: A comparison of radar-determined cloud height and reflected solar radiance measured from the geosynchronous satellite ATS-3. J. Appl. Meteor., 12, 1082-1085.
- Roth, R. C., 1969: A data selection procedure for the rectification and mapping of digitized data. Air Weather Service, AFGWC Tech. Memo. 69-1, Offutt Air Force Base, NB, 20 pp.
- Scofield, R. A., 1978a: Using satellite imagery to estimate rainfall during the Johnstown rainstorm. Preprint Conf. on Flash Floods: Hydrometeorological Aspects, Los Angeles, CA, Amer. Meteor. Soc., May, 1978, 181-189.
- , 1978b: Using satellite imagery to detect and estimate rainfall from flash-flood producing thunderstorms. Preprint Conf. on Weather Forecasting and Analysis and Aviation Meteorology, Silver Spring, MD, Amer. Meteor. Soc., October, 1978, 132-141.
- , and V. J. Oliver, 1977: A scheme for estimating convective rainfall from satellite imagery. NOAA Tech Memo. NESS 86, Washington, D.C., 47 pp.
- Sikdar, D. N., 1972: ATS-3 observed cloud brightness field relate to a mesosynoptic scale rainfall pattern. Tellus, 24, 400-412.
- Simpson, J., and W. L. Woodley, 1971: Seeding cumulus in Florida: new 1970 results. Science, 172, 117-126.

- Weiss, C. E., 1978: Cloud-location corrections near the horizon of an SMS image. NWS/NESS Satellite Applications Info. Note 78/8, Washington, D.C., 8 pp.
- Wolf, D. E., R. M. Endlich, and D. J. Hall, 1972: Further development of objective methods for registering landmarks and determining cloud motions from satellite data. Stanford Research Institute Project 1005, Menlo Park, CA, 76 pp.
- Woodley, W. L., B. Sancho, and A. H. Miller, 1972: Rainfall estimation from satellite cloud photographs. NOAA Tech. Memo. ERL OD-11, Boulder, CO, 43 pp.
- Young, J. T., 1978: Private Communication.

APPENDIX A

This appendix outlines the approach used to relate the digital count values to the rainfall rate in $\text{mm } \frac{1}{2}\text{h}^{-1}$. Most of the information herein was adapted for use with digital GOES-1 infrared data and is based on the rainfall estimation scheme of Scofield and Oliver (1977).

When the attempt was made to adjust step 4 of the Scofield and Oliver decision tree, it became obvious that various variables would have to be converted to make them usable for this study. These included the rainfall rates versus various conditions of cloud growth, the M_B enhancement curve segments, and finally the cloud growth rates. Each of these will be discussed and then the adaptation of step 4 of the Scofield and Oliver decision tree will be presented.

The rainfall rates were converted to $\text{mm } \frac{1}{2}\text{h}^{-1}$ from $\text{in } \frac{1}{2}\text{h}^{-1}$. This was a simple task that required careful conversions into mm for each of the segments and various cloud growth conditions. After some experimentation with the digital data had taken place, it was determined that some small adjustments downward were necessary for the "no change" (or count value not less than 208) category. Basically, however, very little compensation such as this was made to the rest of the breakdown.

Next, the M_B enhancement curve segments, which are given as temperatures only, were converted to digital count values. Since each segment of the M_B curve covered more than one digital count value, it was necessary to determine just how to relate the count values to

rainfall rates at various cloud growth stages. It was decided to spread the digital count values over that particular segment of a specified rainfall rate endorsed by Scofield and Oliver in step 4 of their estimation scheme. For instance, if the segment had the equivalent of 4 digital counts (e.g., varied over 4°C) and the rainfall rate (for a particular cloud growth rate) increased by $2 \text{ mm } \frac{1}{2}\text{h}^{-1}$ from the last segment, each digital count rainfall would be equivalent to $0.5 \text{ mm } \frac{1}{2}\text{h}^{-1}$. By the same token, if the change was $4 \text{ mm } \frac{1}{2}\text{h}^{-1}$, each digital count value at that cloud growth rate level would represent $1 \text{ mm } \frac{1}{2}\text{h}^{-1}$. The digital count value versus rainfall rate breakdown was devised following this logical procedure.

The final variable of interest was the cloud growth rate and how it related to the digital count values. Since the imagery scheme developed by Scofield and Oliver produced fairly good results, these same limits for cloud growth (anvil growth) were maintained for this investigation (e.g., an expansion in size of $2/3^{\circ}\text{Lat}$, approximately 75 km in $\frac{1}{2} \text{ h}$). Some adjustment of this variable may be required in further studies.

Fig. 30 lists the breakdown of digital count values versus rainfall in $\text{mm } \frac{1}{2}\text{h}^{-1}$ and their variance with respect to cloud (anvil) growth rates. These variables were adjusted as little as possible and were adapted almost directly from the imagery scheme of Scofield and Oliver. A quick comparison of Fig. 30 with Fig. 24 (p. 58) will disclose that the rainfall rates for the digital count values from 208-213 were averaged for the cloud growth columns. This was done to

Digital Count Value	Increase in major axis of Anvil (along major axis of contour)			Digital Count Value Same or Decreased to not less than the 208 count value	Decayed to less than 208 count value
	>75 km	38-75 km	≤ 37 km		
177-186	3.0	2.0	1.0	0.5	Trace ↓
187-197	6.0	2.5	2.0	0.5	
198-199	7.0	3.0	2.0	0.5	
200-201	8.0	4.0	2.0	1.0	
202-203	9.0	5.0	2.5	1.0	
204-205	9.5	6.0	2.5	1.0	
206-207	10.0	7.0	3.0	1.0	
208	10.5	7.5	3.5	2.0	
209	11.0	7.5	3.5	2.0	
210	11.5	7.5	3.5	2.0	
211	12.0	8.0	3.5	2.0	
212	12.5	8.0	3.5	2.0	
213	13.0	8.0	3.5	2.0	
214	13.5	8.5	4.0	3.0	
215	14.0	8.5	4.0	3.0	
216	14.5	8.5	5.0	3.0	
217	15.0	8.5	5.0	4.0	
218	15.5	8.5	5.0	4.0	
219	16.0	9.0	6.0	4.0	
220	16.5	9.0	6.0	4.5	
221	17.0	9.0	6.0	4.5	
222	17.5	9.0	6.0	4.5	
223	18.0	9.0	6.0	4.5	
224	18.5	9.0	6.0	4.5	
225	19.0	9.0	6.0	4.5	

Fig. 30. Rainfall rates in $\text{mm } \frac{1}{4}\text{h}^{-1}$ based on the growth or decay of the area of digital count value (adapted from Scofield and Oliver, 1977). This figure was the basis for Fig. 24 (p. 58).

allow an easier analysis of the DCVMs. When computer techniques are developed for this rainfall estimation scheme using digital data, even more expanded versions of Fig. 30 will be possible.

Readers with further interest or questions regarding the technique used here may wish to refer to the paper by Scofield and Oliver (1977) for a more concise explanation of their work.

APPENDIX B

CLOUD TOP DISPLACEMENT CORRECTIONS TOWARD SATELLITE SUBPOINT

The appendix is provided for readers not familiar with the necessity to correct cloud top positions on satellite imagery. All information present below is from Weiss (1978).

Accurate positioning of cloud features on GOES imagery is dependent upon the height of the cloud tops and their distance from the satellite subpoint (SSP). The apparent cloud location and the actual location coincide only over the SSP. Otherwise, the distance from the SSP increases due to earth's curvature and nadir angle. Fig. 31 illustrates this problem. Therefore, for an individual to locate accurately a cloud on GOES imagery, he must apply a correction for earth curvature and nadir angle to obtain the appropriate displacement toward the SSP.

The dimensions used for determining the cloud displacements are shown in Fig. 32. Angle ϕ_s is the great circle arc from the SSP to the cloud's apparent location on the image, h is the height of the cloud above the surface of earth, \bar{R} is the mean earth radius, \bar{R}_e is the mean equatorial radius, \bar{A} is the mean GOES altitude, and d is the location correction (the distance measured along the curved surface of earth). The additional angles in Fig. 32 (β , δ , ϵ , and η) are utilized to calculate d .

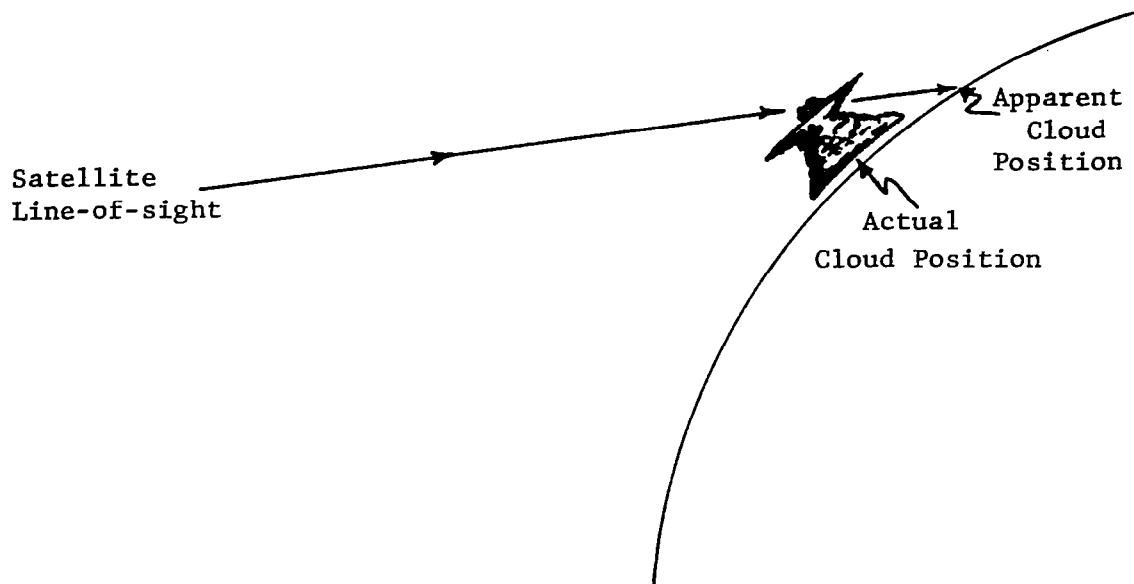


Fig. 31. Diagram illustrating an actual versus an apparent cloud location (after Weiss, 1978).

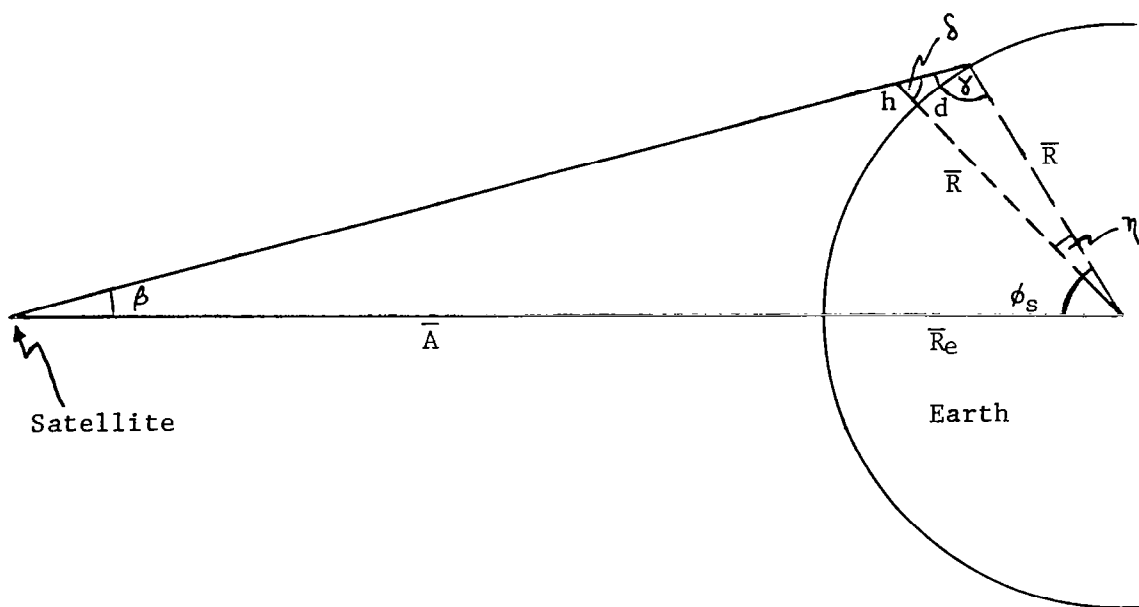


Fig. 32. Dimensions used in calculating cloud location corrections (after Weiss, 1978).

To clear up possible confusion dealing with the mathematics, the sample calculation for a great circle arc of approximately 37° (the approximate interval from the SSP to CLL) is offered.

$$\bar{R} = 6371 \text{ km}$$

$$\bar{R}_e = 6378 \text{ km}$$

$$\phi_s = 37^\circ$$

$$\bar{A} = 35,793 \text{ km}$$

$$h = 13 \text{ km}$$

For triangle $\gamma\beta\phi_s$, we can write

$$\begin{aligned} \tan \frac{1}{2}(\beta - \gamma) &= \frac{\bar{R} - (\bar{R}_e + \bar{A})}{\bar{R} + (\bar{R}_e + \bar{A})} \tan \frac{1}{2}(\beta + \gamma) \\ &= -0.737506 \tan \frac{1}{2}(\beta + \gamma). \end{aligned} \quad (1)$$

Since the sum of interior angles of a triangle equals 180° , we have for triangle $\gamma\beta\phi_s$

$$\beta + \gamma + \phi_s = 180^\circ \quad (2)$$

and for $\beta + \gamma$, we have

$$\beta + \gamma = 180^\circ - \phi_s = 143^\circ \quad (3)$$

By substituting (2) and (3) into (1), we can write

$$\tan \frac{1}{2}(\beta - \gamma) = -0.737506 \tan \frac{1}{2}(180^\circ - \phi_s). \quad (4)$$

We are given that $\phi_s = 37^\circ$, so

$$\tan \frac{1}{2}(\beta - \gamma) = -2.204172. \quad (5)$$

Evaluating (5) gives us

$$\beta - \gamma = -131.193826^\circ. \quad (6)$$

Now, from (3) we have

$$\beta + \gamma = 143^\circ.$$

By adding (3) to (6) we get

$$\begin{array}{r} \beta - \gamma = -131.193826^\circ \\ \beta + \gamma = 143.000000^\circ \\ \hline 2\beta = 11.806174^\circ. \end{array}$$

Therefore

$$\beta = 5.903087^\circ. \quad (7)$$

By solving (3) for γ , we have

$$\gamma = 180^\circ - (\phi_s + \beta) = 137.096913^\circ. \quad (8)$$

The law of sines for triangle $\delta\gamma\eta$ gives

$$\frac{h + \bar{R}}{\sin \gamma} = \frac{\bar{R}}{\sin \delta}. \quad (9)$$

Solving (9) for δ yields

$$\begin{aligned} \sin \delta &= 0.679374 \\ \delta &= \arcsin (0.679374) = 42.794750^\circ. \end{aligned} \quad (10)$$

For triangle $\delta\gamma\eta$, summing the interior angles we have

$$\delta + \gamma + \eta = 180^\circ. \quad (11)$$

Solving (11) for η gives

$$\eta = 0.108337^\circ. \quad (12)$$

Finally arc length d is given by

$$d = \frac{\pi \bar{R} \eta}{180^\circ} = 12.046471 \text{ km.}$$

Thus, for average heights of 13 km at a great circle arc of approximately 37° , the displacement correction of the cloud tops is 12 km toward the SSP.

1. REPORT NO. NASA RP-1034		2. GOVERNMENT ACCESSION NO.		3. RECIPIENT'S CATALOG NO.	
4. TITLE AND SUBTITLE Convective Rainfall Estimation from Digital GOES-1 Infrared Data				5. REPORT DATE September 1979	
				6. PERFORMING ORGANIZATION CODE	
7. AUTHOR(S) Gary L. Sickler* and Aylmer H. Thompson**				8. PERFORMING ORGANIZATION REPORT #	
9. PERFORMING ORGANIZATION NAME AND ADDRESS Department of Meteorology Texas A&M University College Station, Texas 77843				10. WORK UNIT NO. M-288	
				11. CONTRACT OR GRANT NO.	
				13. TYPE OF REPORT & PERIOD COVERED Reference Publication	
12. SPONSORING AGENCY NAME AND ADDRESS National Aeronautics and Space Administration Washington, D. C. 20546				14. SPONSORING AGENCY CODE	
15. SUPPLEMENTARY NOTES This report is based on a study accomplished as a Master of Science thesis at Texas A&M University.					
16. ABSTRACT An investigation was conducted to determine the feasibility of developing an objective technique for estimating convective rainfall from digital GOES-1 infrared data. The study area was a 240 km by 240 km box centered on College Station, Texas (Texas A&M University). The Scofield and Oliver (1977) rainfall estimation scheme was adapted for this study and used with the digital geostationary satellite data. The concept of enhancement curves with respect to rainfall approximation is discussed. Rainage rainfall analyses and satellite-derived rainfall estimation analyses were compared. The correlation for the station data pairs (observed versus estimated rainfall amounts) for the convective portion of the storm was 0.92. This investigation demonstrated that a fairly accurate objective rainfall technique using digital geostationary infrared satellite data is feasible. The rawinsonde and some synoptic data that were used in this investigation came from NASA's Atmospheric Variability Experiment, AVE VII. *Graduate Student; Capt. Sickler's present address is P.O. Box 8791, Langley AFB, VA 23665. **Professor of Meteorology, Texas A&M University, College Station, TX 77843					
17. KEY WORDS			18. DISTRIBUTION STATEMENT STAR Category 47		
19. SECURITY CLASSIF. (of this report) Unclassified		20. SECURITY CLASSIF. (of this page) Unclassified		21. NO. OF PAGES 95	
				22. PRICE	

* For sale by the National Technical Information Service, Springfield, Virginia 22161